

Technical University of Denmark



Heat and water transport in soils and across the soil-atmosphere interface: 2. Numerical analysis

Fetzer, Thomas; Vanderborght, Jan; Mosthaf, Klaus; Smits, Kathleen M.; Helmig, Rainer

Published in:
Water Resources Research

Link to article, DOI:
[10.1002/2016WR019983](https://doi.org/10.1002/2016WR019983)

Publication date:
2017

Document Version
Peer reviewed version

[Link back to DTU Orbit](#)

Citation (APA):
Fetzer, T., Vanderborght, J., Mosthaf, K., Smits, K. M., & Helmig, R. (2017). Heat and water transport in soils and across the soil-atmosphere interface: 2. Numerical analysis. *Water Resources Research*, 53(2), 1080-1100. DOI: 10.1002/2016WR019983

DTU Library

Technical Information Center of Denmark

General rights

Copyright and moral rights for the publications made accessible in the public portal are retained by the authors and/or other copyright owners and it is a condition of accessing publications that users recognise and abide by the legal requirements associated with these rights.

- Users may download and print one copy of any publication from the public portal for the purpose of private study or research.
- You may not further distribute the material or use it for any profit-making activity or commercial gain
- You may freely distribute the URL identifying the publication in the public portal

If you believe that this document breaches copyright please contact us providing details, and we will remove access to the work immediately and investigate your claim.

1 **Heat and water transport in soils and across the soil-**
2 **atmosphere interface – Part 2: Numerical analysis.**

3

4 Thomas Fetzer¹, Jan Vanderborght^{2,3*}, Klaus Mosthaf⁴, Kathleen Smits⁵, Rainer Helmig¹.

5

6 ¹ Institute for Modelling Hydraulic and Environmental Systems, University of Stuttgart,

7 Pfaffenwaldring 61, 70569 Stuttgart, Germany. Thomas.Fetzer@iws.uni-stuttgart.de,

8 Rainer.Helmig@iws.uni-stuttgart.de

9

10 ² Agrosphere Institute, IBG-3, Forschungszentrum Jülich GmbH, D-52425 Jülich, Germany.

11 j.vanderborght@fz-juelich.de

12

13 ³ Centre for High-Performance Scientific Computing in Terrestrial Systems, HPSC TerrSys,

14 Geoverbund ABCJ, Forschungszentrum Jülich GmbH, D-52425 Jülich.

15

16 ⁴ DTU ENVIRONMENT, Department of Environmental Engineering, Technical University of

17 Denmark, Bygningstorvet, Building 115, 2800 Kgs. Lyngby, Denmark. klmos@env.dtu.dk

18

19 ⁵ Center for Experimental Study of Subsurface Environmental processes, Department of Civil

20 & Environmental Engineering, Colorado Schools of Mines, 1500 Illinois Street, Golden, CO

21 80401, USA. ksmits@mines.edu

22

23 * corresponding author

24

25 **Abstract**

- 26 • We evaluate different concepts to describe soil evaporation using numerical
27 simulations.
- 28 • Lateral transport in both soil and atmosphere determine local evaporation from
29 heterogeneous surfaces.
- 30 • Different parameterizations of vapor transport mainly affect diurnal dynamics of
31 evaporation.
- 32

33 **Abstract**

34 In an accompanying paper, we presented an overview of a wide variety of modeling concepts,
35 varying in complexity, used to describe evaporation from soil. Using theoretical analyses, we
36 explained the simplifications and parameterizations in the different approaches. In this paper,
37 we numerically evaluate the consequences of these simplifications and parameterizations. Two
38 sets of simulations were performed. The first set investigates lateral variations in vertical fluxes,
39 which emerge from both homogeneous and heterogeneous porous media, and their importance
40 to capturing evaporation behavior. When evaporation decreases from parts of the heterogeneous
41 soil surface, lateral flow and transport processes in the free flow and in the porous medium
42 generate feedbacks that enhance evaporation from wet surface areas. In the second set of
43 simulations we assume that the vertical fluxes do not vary considerably in the simulation
44 domain and represent the system using one dimensional models which also consider dynamic
45 forcing of the evaporation process, e.g. due to diurnal variations in net radiation. Simulated
46 evaporation fluxes subjected to dynamic forcing differed considerably between model concepts
47 depending on how vapor transport in the air phase and the interaction at the interface between
48 the free flow and porous medium were represented or parameterized. However, simulated
49 cumulative evaporation losses from initially wet soil profiles were very similar between model
50 concepts and mainly controlled by the desorptivity, S_{evap} , of the porous medium, which depends
51 mainly on the liquid flow properties of the porous medium.

52

53 **Introduction**

54

55 In an accompanying paper, Vanderborght et al, (P1) we presented an overview of different
56 concepts and theories commonly used to describe evaporation from soil surfaces and derived
57 simplifications of more comprehensive descriptions of the flow and transport processes. The
58 main objective of this paper is to evaluate the consequences of model simplifications by
59 performing exemplary simulations. The setup of these simulations is based on the outcome of
60 P1 in which we identified three main groups of options for model simplifications. The first
61 group deals with the dimensions of the process description (1D vs 2/3D) which depends on the
62 decision to consider or neglect lateral fluxes and gradients in state. The second group is related
63 to the description of vapor transport in the porous medium and the third group to the
64 representation of the interaction between the porous medium and the free flow. The first set of
65 simulations addresses option 1 and evaluates the effect of lateral variations in the porous
66 medium properties and the coupling between lateral flow and transport processes in the porous
67 medium and the free flow on evaporation processes.

68 In the second set of simulations, to further investigate the effect of options 2 and 3, we assume
69 a homogeneously evaporating surface and ignore any lateral variations thus representing the
70 system in one-dimension. In these simulations, the exchange between the porous medium and
71 the free-flow is derived from the vertical gradients in state variables in the free flow using
72 transfer resistances. Using this set of simulations, the effect of the representation of the vapor
73 flow in the porous medium and the representation of the interaction between the porous medium
74 and the free-flow is evaluated. A simplified version of the 1-D model is then used to obtain
75 (approximate) analytical expressions. We illustrate how these expressions can be used to
76 evaluate model simplifications. Comparing simulation results, we then draw conclusions about
77 the type of data or observations required to properly parameterize models of different

78 complexity. This paper focusses on *qualitative* differences between modeling approaches to
79 specifically address the question whether different model concepts lead to fundamental
80 differences in fluxes dynamics that cannot be matched by changing the model parameters. A
81 direct and *quantitative* comparison between simulation results and experimental observations,
82 which also needs to address the parameterization problem, will be the focus of future work but
83 is out of the scope of this paper .

84

85

86 **Flow and transport properties of the considered porous** 87 **media .**

88

89

90 Two soil types were considered: a finer textured silt and a coarser textured sandy loam. The
91 hydraulic properties were described by the Mualem van Genuchten functions [*van Genuchten*,
92 1980] and the parameters of the hydraulic functions are given in Table 1. To appraise the
93 relevance of liquid and vapor fluxes for different soil water pressure heads, ψ [m], the hydraulic
94 conductivity curves for the isothermal liquid $K_{l,\psi}$ [m s^{-1}] and vapor conductivity $K_{v,\psi}$ [m s^{-1}] at
95 a temperature of 20 °C and 40 °C (only sandy loam soil) are shown in Figure 1. The relations
96 of these conductivities to the fluid viscosity, (relative) permeability, the volumetric air phase
97 content and effective vapor diffusion coefficient in the porous medium, pressure head, relative
98 air humidity, and temperature are given in Eqs. [21,22] of P1. The effective vapor diffusion
99 coefficient in the porous medium was described using the Millington Quirk equation
100 [*Millington and Quirk*, 1961]. The conductivity curves illustrate that in the sandy loam soil, the
101 vapor conductivity becomes more important than the liquid conductivity for pressure heads

102 smaller than -30 m ($\approx -300 \text{ kPa}$) whereas for the silt soil, the liquid conductivity is more
103 important for pressure heads larger than $-2 \cdot 10^3 \text{ m}$ ($\approx -20 \text{ MPa}$). At 40° C , the liquid and vapor
104 conductivities are respectively 1.5 and 3 times higher than at 20° C demonstrating the relative
105 contribution of vapor transport at higher temperatures.

106

107 **Simulation set 1: Effect of Lateral Transfer Processes**

108 **Model and scenario description.**

109 Simulations in the first set were performed using the two-phase two-component porous medium
110 model that is coupled with the Reynolds-averaged Navier-Stokes (RANS) free flow model.
111 Simulations were carried out using the open-source simulator DuMu^x [Flemisch et al., 2011;
112 Schwenck et al., 2015], which is based on the numerical toolbox DUNE [Bastian et al., 2008a;
113 Bastian et al., 2008b]. The equations were discretized fully implicitly in time and using the
114 box-method in space [Baber et al., 2012; Helmig and Huber, 1998].

115 The scenarios varied the length of the domain (e.g. short vs long test sections) and lateral
116 variations in the porous medium properties (e.g. homogeneous versus heterogeneous) As
117 demonstrated below, both variations led to lateral variations in state variables in the free flow,
118 lateral fluxes in the porous medium and lateral variations in the vertical fluxes at the porous
119 medium-free flow interface.

120 Boundary conditions (wind speed, air temperature and humidity of inflowing air) were kept
121 constant in time.

122

123 **Effect of soil sample length and wind speed on evaporation: impact of** 124 **gradients in the free flow.**

125 In the first scenario, the effect of the length of a wet soil patch downstream of a uniform and
126 constant dry air flow on the evaporation rate for different wind speeds ($0.5 - 5 \text{ m s}^{-1}$) was

127 simulated. Specifications of the simulation domain, discretization, initial and boundary
128 conditions are given in Figure 2.

129 As shown in Figure 3, the average evaporation rate from a wet patch clearly increased with
130 decreasing patch size. In addition, the evaporation rate increased with increasing wind speeds
131 and the relative increase of evaporation with decreasing patch size was similar for different
132 wind speeds, except for the smallest patch sizes. The larger patches had lower evaporation than
133 the small patches based on the changes in the free flow humidity. Because the air was more
134 saturated with water vapor when it flows along the downstream section of the larger patch, the
135 evaporation rate for the downstream section was lower, making the overall evaporation rate
136 lower. This illustrates the effect of lateral variations in relative air humidity, temperature, and
137 wind speed that emerge above an evaporating surface with finite length on the exchange
138 process.

139

140 **Effect of soil heterogeneity on evaporation.**

141 To investigate the effect of soil type (i.e. silt and sandy loam) and orientation on evaporation,
142 simulations were run in which two soil blocks were placed adjacent to each other as seen in
143 Figure 4. In the first test case, the silt block was placed upstream (left) from the sandy loam
144 block and vice versa for the other cases while for the second case, the silt block was placed
145 downstream (right). In a third case, a homogeneous silt block was considered. To evaluate the
146 influence of lateral liquid and heat fluxes within the porous medium, we considered a fourth
147 and a fifth set of simulations in which either lateral water or heat fluxes between the two blocks
148 were blocked.

149 **Impact of heterogeneities in the porous medium**

150 Figure 5 shows the evaporation rates from the homogeneous and heterogeneous test cases. For
151 the homogeneous silt case, a steady state evaporation rate was obtained during the first day that
152 remained constant until day 3 when the evaporation rate decreased. As expected from the free

153 flow and porous medium flow coupling resulting in feedbacks to the atmosphere and higher
154 humidities as the air flows from the downstream to the upstream portions of the test section, the
155 evaporation rate from the downstream half of the test section was smaller than from the
156 upstream half. The evaporation rate from the upstream part decreased a little earlier than the
157 downstream part, which led to a short peak in evaporation from the downstream part. Since the
158 initial water distribution was uniform in the simulation domain, this illustrates that lateral water
159 flow in the porous medium compensated for the higher evaporation losses in the upstream part.
160 Lateral variations in air humidity and temperature in the free flow, which led to lateral variations
161 in evaporation rate, also induced lateral liquid flow in the porous medium. These lateral fluxes
162 effectively homogenized the effect of spatial variations of fluxes at the porous medium surface
163 so that the homogeneous porous medium could have been represented by a 1-D vertical profile.
164 In the heterogeneous test cases (i.e. silt and sandy loam, see Figure 4) the evaporation rates
165 from both the silt and sandy loam were initially the same. When the water content at the soil
166 surface is sufficiently high, the vapor pressure at the soil surface is close to the saturated vapor
167 pressure and the evaporation is controlled by the atmospheric conditions and the surface
168 roughness, oftentimes referred to as stage I evaporation, but not by the porous medium
169 hydraulic properties. However, the sandy loam section's evaporation rate started to decrease
170 earlier than evaporation from the finer silty part, related to the differences in soil hydraulic
171 properties. This falling rate period correlates to the soil entering into stage II evaporation.
172 The decrease in evaporation from the sandy loam part occurred in two steps in this example.
173 The first gradual decrease occurred as the surface of the sandy loam was dried out and the
174 residual water content was (Figure 6). During this time, the finer silt material continued to
175 evaporate at a high rate and did not dry out. The silt material functioned as a wick that drained
176 water from the adjacent sandy loam resulting in a longer sustained high evaporation from the
177 silt material than in the homogeneous silty test case. This behavior was also demonstrated in

178 lab experiments [*Lehmann and Or, 2009*]. The decrease in evaporation from the sandy loam
179 was accompanied by an increase in evaporation from the silt part.

180 The second smaller decrease in evaporation rate from the sandy loam occurred when the liquid
181 water flow to the evaporation front in the sandy loam soil driven by gradients in capillary forces
182 was reduced by the limited water supply due to the no-flow bottom boundary condition of the
183 box. With a deeper porous-medium box the decrease would be continuous. After the second
184 decrease of evaporation from the sandy loam, also the silt started drying out. Also the second
185 drop in evaporation rate from the sandy loam surface corresponded with a further increase in
186 evaporation rate from the silt surface, despite the drying of the silt surface. This shows that for
187 a heterogeneous surface, the evaporation rate may locally increase and become even larger than
188 from a homogeneous surface. The increase in evaporation from the silt part was larger when it
189 was located downstream of the sandy loam part. In this case, the temperature and humidity of
190 the air that flowed over the silt part, respectively, increased and decreased when the evaporation
191 from the upwind part decreased.

192 When the finer silt part was upstream of the sandy loam, the evaporation rate from the silt also
193 increased when evaporation from the sandy loam part decreased. This indicates that, in this
194 case, lateral mixing in the air increased temperature and reduced humidity in the upwind
195 direction above the silt part. Another potential reason is the lateral heat flux in the porous
196 medium, which increases the temperature at the surface of the silt soil when evaporation from
197 the sandy loam part ceased.

198

199 **Impact of changing lateral gradients in the free flow above drying heterogeneous porous media**

200 To evaluate the influence of changes in lateral gradients in the free flow above a drying
201 heterogeneous porous medium on the evaporation, we derived in a first step 1-D aerodynamic
202 resistances (Table 2), r_V [$s\ m^{-1}$] for the upstream and downstream part of the homogeneous
203 porous medium using:

$$r_V = \frac{\bar{\rho}_g^w(z=0) - \rho_{g,inflow}^w}{\bar{F}_w} \quad [1]$$

204

205 where and $\rho_{g,inflow}^w$ [kg m⁻³] is the vapor concentration in the inflowing air, $\bar{\rho}_g^w(z=0)$ the
 206 average vapor concentration at the interface in the up or downstream part and \bar{F}_w [kg m⁻² s⁻¹]
 207 the average vapor flux from the up or downstream part. The vapor concentrations and fluxes
 208 during stage I evaporation were used to calculate the r_V 's. These r_V 's were subsequently used
 209 to calculate the evaporation rates from the heterogeneous porous medium using the vapor
 210 concentrations in the inflowing air and at the soil surface of the up- and downstream parts when
 211 evaporation of one of the parts ceased (Table 2), which influenced the lateral gradients in air
 212 humidity and temperature.

213 For the upstream part, the evaporation rates were fairly well reproduced using the 1-D
 214 aerodynamic resistance (see Table 2). This indicates that the air humidity and air temperature
 215 profiles in the upstream part are mainly defined by the vapor concentration and temperature at
 216 the porous medium surface and in the inflowing air. The increase in evaporation rate from the
 217 upstream silt part when the evaporation from the downstream sandy loam part ceased could be
 218 linked to an increase in vapor concentration and temperature at the porous medium surface.
 219 Whether this increase in surface temperature and vapor concentration can be predicted based
 220 on the lateral heat transfer in the porous medium alone still needs to be investigated. When the
 221 dry and less-evaporating sandy loam part was upstream, its lower evaporation rate could also
 222 be reproduced fairly well from the surface vapor concentration and the 1-D aerodynamic
 223 resistance.

224 The conditions in the free flow in the downstream part, i.e. vertical profiles of air humidity and
 225 temperature, were strongly influenced by evaporation from the upstream part and changed when
 226 the evaporation from this part changed. These temporal changes in air humidity profiles due to
 227 changing evaporation rates in upstream parts from heterogeneous surfaces could not be

228 represented by 1-D aerodynamic resistances that were derived for other evaporation conditions
229 in the upstream part.

230

231 **Impact of lateral water and heat fluxes in the porous medium**

232 Figure 7 shows simulated evaporation rates for the case that lateral water flow between up- and
233 downstream parts is blocked. For the homogeneous setup, blocking of lateral water flow
234 between the up- and downstream parts led in the upstream part to an earlier transition to stage-
235 II evaporation compared with the case in which lateral water flow between the two parts could
236 take place (compare Figure 5 and Figure 7). The decrease in evaporation from the upstream part
237 led to a lower air humidity above the downstream part and an increase in evaporation from the
238 downstream part. For the heterogeneous setups, the switch to stage-II evaporation occurred
239 earlier in the silty material, which could not rely on liquid water transfer from the sandy loam,
240 and later in the sandy loam material, compared to the cases where lateral water transfer between
241 the two parts could take place.

242 In Figure 8, simulated evaporation rates are shown for the case that conductive heat transfer
243 between up and downstream parts are blocked but lateral water flow is allowed. These
244 simulation results show more similarities with the fully coupled simulation results (compare
245 Figure 5 and Figure 8). However, the increase in evaporation from the silt part at the time when
246 the evaporation from the sandy loam part decreased was clearly less than for the case also lateral
247 conductive heat fluxes in the porous medium were considered. This is especially clear when the
248 silt part is located upstream of the sandy loam part. When conductive heat transfer between the
249 silt and sandy loam blocks was blocked, the evaporation rate in the upstream silt block did not
250 increase when the evaporation from the downstream sandy loam part decreased (Figure 8) and
251 its temperature increased. This demonstrates that the increase in evaporation from the upstream
252 silt part when the evaporation from the downstream sandy loam part decreased and that was

253 simulated by the full model (Figure 5) was due to conductive heat fluxes in the porous medium
254 rather than heat transfer through the air flow.

255

256 **Simulation set 2: Dynamic Forcing of Evaporation**

257 **Used models and considered simulations.**

258 In this example, the effect of different model concepts on simulated evaporation from a
259 homogeneous surface under dynamic forcing is investigated. In contrast to the previous
260 example, lateral variations in state variables and in vertical fluxes at the porous medium-free
261 flow interface were assumed to be negligible so that the flow and transport process in the porous
262 medium could be represented as a 1-D process. The transfer or fluxes of water and heat between
263 the porous medium and the free flow could be described using transfer resistances, the vapor
264 concentrations and temperatures at the porous medium-free flow interface, and at a reference
265 height in the free flow (Eq. [1]). The transfer resistances depend on the wind profile, which for
266 a homogeneous surface can be represented by a logarithmic profile, and on the roughness of
267 the surface (see Eqs. 50, 51, 57 and 58 in P1). The fluxes between the porous medium and the
268 free flow were then used as boundary conditions to solve the water and heat balance equations
269 in the porous medium. Furthermore, vertical gas phase fluxes in the porous medium were
270 neglected so as the transport of the dry air component. The most comprehensive model for this
271 simulation set was the one component (water) one-and-a-half phase (liquid phase and only
272 diffusion in the gas phase) model (for details see P1) that is coupled with the heat flow equation.
273 We will call this model also the non-isothermal vapor-water flow model.

274 Simulations by this model were compared to simulations with the Richards equation which only
275 considers isothermal flow and transport of the component water in the liquid phase (isothermal,
276 one component, one phase) that is decoupled from the heat flux in the porous medium. For a
277 sufficiently wet soil surface when the vapor concentration is close to the saturated vapor

278 concentration, the coupling of the Richards equation with the heat fluxes is done at the free-
279 flow porous medium interface where a surface energy balance is solved to determine the
280 potential evaporation flux across the surface, i.e. the stage I evaporation rate. This potential
281 evaporation rate was used a flux boundary condition for the Richards equation. This surface
282 heat balance uses the same transfer resistances for vapor and sensible heat transfer in the free
283 flow as the one component one-and-a-half phase model but assumes that vapor concentration
284 at the surface is always saturated. The reduction of evaporation during stage II evaporation,
285 when the soil surface dries out and the surface vapor concentration is significantly lower than
286 the saturated one, was represented using a threshold formulation of the boundary condition. The
287 flux boundary condition was switched to a constant pressure head boundary condition when the
288 water pressure head at the soil surface reached a critical value, ψ_{crit} . Since the pressure head is
289 kept fixed and independent of other boundary conditions in this model during stage II
290 evaporation, the water fluxes from the deeper soil to the soil surface and the evaporation rate
291 are decoupled from the evaporative forcing (radiation, wind speed, air humidity and
292 temperature). The sensitivity of the simulation results to the choice of ψ_{crit} in soils with different
293 hydraulic properties was evaluated by using an analytical approximation of the Richards
294 equation. This analytical approximation was furthermore used to evaluate the impact of vapor
295 transport under isothermal conditions.

296 An alternative to the threshold boundary condition formulation for the Richards equation is to
297 include a term in the transfer resistance that represents the resistance to vapor transfer from the
298 evaporation surface towards the soil surface. This resistance is accounted for by multiplying
299 the potential evaporation by a β -factor (see Eq. [60] P1) that is a function of the water content
300 of the soil surface. In this model, the evaporation rate during stage II, i.e. when $\beta < 1$, is still
301 coupled to the evaporative forcing through the potential evaporation rate. Therefore, this can
302 be considered to a semi-coupled description. We evaluated how this parameterization depends

303 on the choice of the thickness of the surface layer and on other parameters such as the surface
304 temperature using simulations with the non-isothermal vapor-water flow model.

305 In order to evaluate the sensitivity of the simulation results to vapor transport and processes that
306 influence the parameterization of this transport (e.g. local thermal non equilibrium effects which
307 are represented by an enhancement η of the thermal hydraulic conductivity for vapor transport,
308 K_{vT} ($\text{m}^2 \text{K}^{-1} \text{s}^{-1}$) (See Eq. 24 of P1), turbulent pumping which can be represented by a higher
309 vapor diffusion coefficient), simulations were performed for different sets of parameterizations.

310 **Boundary conditions and simulation setup.**

311 The forcing boundary conditions at the soil surface represent an 11-day period in August 2010
312 at the Selhausen test-site ($50^\circ 52' 47.89'' \text{N}$, $6^\circ 26' 33.14'' \text{E}$) close to Jülich (Germany).
313 Radiation, wind speed, relative humidity, and air temperature measured at 2 m height were
314 assumed to be representative of the entire field (Figure 9). A flat bare soil surface with a
315 roughness height, d , of 2 mm was assumed. The surface albedo was 0.23 and the thermal
316 emissivity of the soil surface was set to 0.9. A soil profile with a depth of 1 m was considered
317 and at the bottom of the soil profile, a constant temperature (15°C) and zero pressure gradient
318 in the liquid phase was assumed. The initial conditions in the two soil profiles with different
319 soil hydraulic properties were defined so that the initial volumetric water content in the profiles
320 was similar, i.e. $\theta \approx 0.2$. Simulations were carried out using Hydrus 1D [*Saito et al.*, 2006;
321 *Šimunek et al.*, 2008; *Šimunek et al.*, 2016] which was slightly changed so that downwelling
322 long wave radiation, surface roughness, and enhancement factors η could be defined by the
323 user.

324

325 **Effect of assuming isothermal processes under dynamic forced** 326 **evaporation.**

327 The potential evaporation rates and simulated evaporation rates from the two soils using the
328 non-isothermal vapor-water flow model (one component, one-and-a-half phase) and the

329 Richards equation with two different boundary condition thresholds: $\psi_{crit} = -10^4$ cm or $\psi_{crit} = -$
330 10^5 cm are shown in Figure 10.. For the same test cases, simulated pressure heads at the soil
331 surface and cumulative evaporation losses are given in Figure 11 and Figure 12, respectively.
332 As expected, for both soils, the simulated evaporation rate of the drying soil surface became
333 smaller than the potential evaporation rate after a certain time (Figure 10). The simulated
334 evaporation rate and cumulative evaporation losses were larger in the silt than in the sandy loam
335 soil (Figure 12).

336 For the Richards equation models, the evaporation rate became smaller than the potential
337 evaporation rate when the threshold pressure head at the surface was reached (stage II). In the
338 non-isothermal vapor-water flow model, this happened due to a simulated decrease in air
339 humidity at the soil surface when the soil surface dried out. For the sandy loam soil, the
340 difference in the simulated evaporation rate and cumulative evaporation losses for the two
341 different threshold pressures is hardly noticeable, whereas for the silt soil, the evaporation rates
342 and cumulated evaporation are noticeably smaller for the larger ψ_{crit} .

343 In the silt soil, the diurnal temporal dynamics of the evaporation rate that was simulated using
344 the non-isothermal vapor-water flow model was well reproduced by the Richards equation.
345 During the morning hours, the actual evaporation rate kept up with the potential evaporation
346 until the soil surface dried out and the evaporative demand could not be maintained by upward
347 flow from deeper in the soil profile. From that moment on, the actual evaporation rate decreased
348 with time and decoupled from the diurnal dynamics of radiation, air temperature and relative
349 air humidity. During the late afternoon or evening, the decreasing radiation and air temperature
350 and increasing air humidity led to a drop in evaporative demand by the atmosphere and the
351 evaporative demand could again be supplied by water fluxes from the soil profile. The lower
352 evaporative demand led to a relaxation of the pressure heads at the soil surface.

353 During night, the soil surface layer was replenished by upward water flow from the deeper soil.
354 In the silt soil during night and a considerable part of the day, the pressure heads at the soil

355 surface were larger than $-2 \cdot 10^5$ cm (Figure 11), i.e. the pressure head below which vapor
356 conductivity, $K_{v,\psi}$, becomes larger than liquid conductivity, $K_{l,\psi}$, (Figure 1) so that evaporation
357 dynamics were closely linked to liquid water fluxes. This explains why the Richards and the
358 non-isothermal water vapor flow model simulate similar evaporation dynamics for this soil.
359 In the sandy loam soil, the diurnal dynamics of the evaporation and the pressure heads during
360 night simulated by the non-isothermal water vapor flow model started deviating between the
361 different models after three days (from DOY 229). From this day, the simulated pressure heads
362 at the soil surface became significantly smaller than $-3 \cdot 10^3$ cm, i.e. the pressure head below
363 which $K_{v,\psi} > K_{l,\psi}$, during the whole day. The diurnal dynamics of evaporation from the soil
364 surface was therefore controlled by vapor transport in the surface soil layer and seemed to be
365 coupled again with the diurnal forcing. When the soil surface is dry, the gradient in water
366 content that drives diffusive water flow cannot increase during the day. During the day, the dry
367 soil surface heats up leading to downwards directed thermal gradients so that the water/vapor
368 flow that is driven by a thermal gradient reduces the evaporation rate during the day. The
369 increase in evaporation during the day must therefore be due to an increase with temperature of
370 the isothermal hydraulic conductivity for liquid, $K_{l,\psi}$, and mainly for vapor transport, $K_{v,\psi}$ (see
371 Figure 1). It is evident that these dynamics cannot be reproduced by an isothermal Richards
372 equation based model with a fixed pressure head at the soil surface.

373

374 **Analytical approximations of the Richards equation to assess the**
375 **influence of vapor transport on cumulative evaporation and to determine**
376 **ψ_{crit} .**

377 Despite the fact that the diurnal dynamics of the evaporation rate in the sandy loam soil were
378 not well reproduced by the Richards equation, the simulated cumulative evaporation rates by
379 the non-isothermal vapor liquid model and Richards equation were still in relatively close
380 agreement (Figure 12), as was also concluded by *Assouline et al.* [2013] and *Milly* [1984]. This

381 suggests that the cumulative evaporative water losses are controlled mainly by the transfer of
 382 liquid water from the deeper soil towards the evaporative front rather than by diffusive vapor
 383 transfer from the evaporative front towards the soil surface. The diurnal dynamics of the
 384 evaporation process, however, are controlled by temperature dependent vapor transfer from the
 385 evaporative front during the day, leading to a drying of the soil surface layer and rewetting of
 386 this layer during night by liquid water flow and vapor condensation [Assouline *et al.*, 2013].
 387 An inspection of the θ -based formulation of the isothermal, one-component, one-and-a-half
 388 phase equation:

$$\frac{\partial \theta}{\partial t} = \frac{\partial}{\partial z} \left(D_w(\theta) \frac{\partial \theta}{\partial z} \right) + \frac{\partial K(\theta)}{\partial z} \quad [2]$$

389
 390 where $\theta = \theta_l + \theta_v$ is the sum of the liquid and vapor water content both expressed as volume
 391 liquid water per bulk volume of soil and water diffusivity D_w ($\text{m}^2 \text{s}^{-1}$) is:

$$D_w = (K_{l,\psi} + K_{v,\psi}) \frac{\partial \psi}{\partial \theta} \quad [3]$$

392
 393 (See Eq. [25] in P1) can be used to explain the similar cumulative evaporation losses that were
 394 simulated by the Richards equation and by the non-isothermal vapor-water flow model. It
 395 allows furthermore (i) evaluating the relative importance of liquid water flow towards an
 396 evaporating surface compared with vapor transport from the evaporating surface towards the
 397 soil-atmosphere interface and (ii) determining a suitable value of the threshold boundary
 398 condition ψ_{crit} for the Richards equation. When flow due to gravity (second term of the right
 399 hand side of Eq. [2]) can be neglected, Eq. [2] can be reduced to an ordinary differential
 400 equation using the Boltzmann transform $\lambda = \frac{|z|}{\sqrt{t}}$:

$$-\frac{\lambda}{2} \frac{d\theta}{d\lambda} = \frac{d}{d\lambda} \left(D_w \frac{d\theta}{d\lambda} \right) \quad [4]$$

401

402 For the case of a uniform initial water content, θ_i which corresponds with $\theta(\lambda=\infty)$, and an
 403 instantaneous reduction of the water content at the soil surface that remains constant over time,
 404 θ_{sur} , which corresponds with $\theta(\lambda=0)$, the solution of Eq. [4] leads to a unique $\theta(\lambda)$ profile. Figure
 405 13 shows that soil moisture profiles simulated by the non-isothermal vapor-water flow fall
 406 nearly on one reference curve when plotted versus the rescaled depth λ . The area between this
 407 reference curve and the horizontal line that corresponds with θ_i , defines the desorptivity S_{evap}
 408 [$\text{m s}^{-0.5}$]:

$$S_{evap} = \int_{\theta_{sur}}^{\theta_i} \lambda(\theta) d\theta = \int_0^{\infty} [\theta_i - \theta(\lambda)] d\lambda \quad [5]$$

409
 410 From a water balance follows directly that the cumulative evaporation, E_{cum} [m], from a soil of
 411 which the soil surface moisture content is instantaneously reduced to a surface water content,
 412 θ_{sur} , that remains constant over time can be described as:

$$E_{cum} = S_{evap} \sqrt{t} \quad [6]$$

413
 414 An instantaneous reduction of the surface water content to a fixed value θ_{sur} is not a realistic
 415 boundary condition. The ‘Time Compression Analysis’ (TCA) can be used to fix this problem.
 416 In TCA, the evaporation process is split in two periods: stage I between $t = 0$ and $t = t_c$ and stage
 417 II $t > t_c$. For stage II, the cumulative evaporation is described using the following adapted form
 418 of Eq. [6]:

$$E_{cum} = S_{evap} \sqrt{t - t_c + t_p} \quad [7]$$

419
 420 where t_p is the time that would be needed to evaporate the same amount of water when the
 421 surface water content is instantaneously dropped to θ_{sur} as during stage I. Similar forms of this
 422 model have been introduced by *Black et al.* [1969], *Boesten and Stroosnijder* [1986], and

423 *Ritchie* [1972]. Figure 12 shows that cumulative evaporation losses can be reproduced relatively
 424 well by this simple model. The crucial parameter in this model is S_{evap} which is related to the
 425 water diffusivity as [Parlange *et al.*, 1985]:

$$S_{evap}^2 = \frac{8}{3} (\theta_i - \theta_{sur})^2 \int_0^1 (1 - \theta) D_w(\theta) d\theta \quad \theta = \frac{\theta - \theta_{sur}}{\theta_i - \theta_{sur}} \quad [8]$$

$$S_{evap}^2 = \frac{8}{3} \int_{\psi_{sur}}^{\psi_i} (\theta_i - \theta(\psi)) (K_{l,\psi}(\psi) + K_{v,\psi}(\psi)) d\psi \quad [9]$$

426
 427 From Eq. [8] follows that the S_{evap}^2 is an integrated or weighted average diffusivity or
 428 conductivity over the range of soil water contents or pressure heads between the soil surface
 429 and water content or pressure head deeper in the soil profile. The effect of vapor transport on
 430 S_{evap} can be evaluated by calculating S_{evap} for $K_{v,\psi} = 0$ whereas the effect of the threshold
 431 pressure head ψ_{crit} can be inferred from calculating S_{evap} for $\psi_{sur} = \psi_{crit}$. In Table 3, S_{evap}
 432 calculated using Eq. [8] for the two different soils are given together with S_{evap} derived from
 433 fitting Eq. [7] to simulated cumulative evaporation (Figure 12). Also included in Table 3 is the
 434 cumulative evaporation during stage II evaporation, E_{cum} , that was simulated by the non-
 435 isothermal vapor-water flow model and by the Richards equation for two different ψ_{crit} . The
 436 calculated S_{evap} indicate that vapor transport had almost no effect on the cumulative evaporation
 437 in the silt soil whereas in the sandy loam soil there was a noticeable effect as was confirmed by
 438 the E_{cum} simulations. However, the effect of thermal gradients is not considered in S_{evap} so that
 439 a perfect correlation between S_{evap} and E_{cum} cannot be expected.

440 For the boundary conditions that we considered, the downwards directed thermal gradients led
 441 to a smaller increase in E_{cum} when using the non-isothermal vapor-water flow model compared
 442 to simulations with the Richards equation than expected from the increase of S_{evap} from
 443 including vapor transport through $K_{v,\psi}$. Also the effect on the simulated cumulative evaporation
 444 of the threshold ψ_{crit} in the two different soils can be evaluated using S_{evap} . For the sandy loam

445 soil, there was no difference in S_{evap} and E_{cum} for $\psi_{crit} = -10^4$ or -10^5 cm whereas S_{evap} and E_{cum}
446 for the silt soil were clearly smaller for $\psi_{crit} = -10^4$ cm than for $\psi_{crit} = -10^5$ cm. This indicates
447 that S_{evap} can be used as an indicator to demonstrate the relevance and importance of vapor flow
448 and to define a suitable critical surface pressure head for a threshold boundary condition. S_{evap}
449 also indicates that vapor transport will gain importance under more arid and warmer conditions.
450 Initially drier soil conditions (smaller ψ_i) and higher soil temperatures (higher $K_{v,\psi}$, see Figure
451 1) will increase the contribution of vapor transport to S_{evap} . But, the effect of temperature
452 gradients that are expected to increase under drier conditions may deteriorate the correlation
453 between S_{evap} and E_{cum} .

454

455 The Boltzmann transform of the diffusion equation can also be used to link the shape of the soil
456 moisture profiles to the shape of $D_w(\theta)$ function. Only when $\frac{dD_w}{d\theta} < 0$, i.e. when D_w increases
457 with decreasing θ , a ‘hooked’ $\theta(\lambda)$ or $\theta(z)$ profile can be obtained, i.e. $\frac{d^2\theta}{d\lambda^2} > 0$ [van Keulen and
458 Hillel, 1974]. Since the effective vapor diffusion coefficient increases with increasing
459 volumetric air content, i.e. when θ decreases, considering vapor flow leads to $\frac{dD_w}{d\theta} < 0$ for small
460 volumetric water content and therefore explains the S-shaped or hooked water content profiles
461 close to the soil surface (Figure 13). When only $K_{l,\psi}$ is considered in D_w , $\frac{dD_w}{d\theta} > 0$, so that the
462 Richards model cannot reproduce hooked $\theta(z)$ profiles (Figure 14). Although the differences in
463 simulated water content profiles close to the soil surface between the non-isothermal vapor
464 water flow model and the Richards model did not have a large impact on the simulated soil
465 water balance, these differences might have important impacts on the interpretation of surface
466 soil moisture contents that are observed by remote sensing [Moghadas *et al.*, 2013]. Monitoring
467 the change of the shape of the soil moisture profile close to the soil surface may be used to
468 determine the time when evaporation shifts from stage I to stage II evaporation. Besides active

469 off-ground radar systems, also portable NMR (nuclear magnetic resonance) systems bear
470 potential to obtain vertical soil moisture profiles with high spatial resolution and can be used
471 determine the shift of the evaporation process from stage I to stage II [Merz *et al.*, 2014; Merz
472 *et al.*, 2015].

473

474 **Profiles of liquid and vapor fluxes, liquid water content, and soil**
475 **temperature.**

476 Figure 15 shows depth profiles of total water fluxes, liquid water fluxes and vapor fluxes during
477 midday at DOY 235.5 that were simulated by the non-isothermal vapor-water flow model.
478 Deeper in the soil profile, the total water flux is dominated by liquid flow whereas close to the
479 soil surface, liquid water flow goes to zero and upward (positive) water vapor flow dominates.
480 The depth at which the upward liquid flow starts gradually decreasing and the vapor flux
481 increasing with height indicates the evaporative front within the soil profile. This evaporation
482 front is not a sharp interface but a transition zone where evaporation in the subsurface takes
483 place, which is also confirmed by experimental observations [Heitman *et al.*, 2008a; Heitman
484 *et al.*, 2008b].

485 After 10 days of evaporation, the evaporative front in both soils was still quite close to the soil
486 surface, at 2-3 mm below the surface in the silt soil and at 1 cm below the surface in the sandy
487 loam soil. In both soils, the upward liquid flow towards the evaporating front was larger than
488 the evaporation rate at the soil surface. Part of the evaporating water is transported back into
489 the deeper soil by vapor flow, which is negative and downward below the evaporating surface.
490 The evaporation front corresponds with the bend in the soil moisture profiles close to the soil
491 surface that are simulated by the non-isothermal vapor liquid flow model.

492

493 The evaporation front below the soil surface also left an imprint on the soil temperature profile
494 with a larger temperature gradient above than below the evaporation front, which functions as

495 a sink term for heat flow (Figure 16). This sink term, which can be derived from measured
496 temperature profiles with a high vertical resolution combined with estimates of soil thermal
497 properties may be used to estimate the soil evaporation rate (e.g. [Heitman *et al.*, 2008a;
498 Heitman *et al.*, 2008b; Sakai *et al.*, 2011]).

499 Soil surface or skin temperatures are closely linked to soil evaporation, which depends during
500 stage II, in part, on soil hydraulic properties. Figure 17 shows simulated soil surface
501 temperatures of the drying silt and sandy loam soils, of a wet silt soil surface, and of the air
502 temperature, which was used as a boundary condition. When the evaporation rate started
503 deviating from the potential evaporation, i.e. after about 0.5 days in the sandy loam and 1.5
504 days in the silt soil (Figure 10), the soil surface temperature of the drying soils became higher
505 than that of a wet soil surface. The time for the onset of the transition from stage I to stage II
506 evaporation, as well as the degree with which the evaporation rate and consequently the soil
507 surface temperature deviate from the wet soil surface, differed between the two different soils.

508 Soil surface temperatures of the sand-loam soil started increasing faster and to a larger extent
509 than those of the silt soil. The different hydraulic behavior of the two soils led to differences in
510 soil surface temperature of up to 10 °C. Monitoring soil surface temperature may therefore be
511 used to identify soil hydraulic properties (e.g. [Chanzy *et al.*, 1995; Steenpass *et al.*, 2010]) or
512 to identify when evaporation shifts from stage I to stage II [Tolk *et al.*, 2015].

513 It should be noted though that the hydraulic properties of the soil surface layer may differ
514 considerably from those of the subsoil due to soil tillage [Steenpass *et al.*, 2010]. Soil tillage
515 may also affect the roughness of the soil surface and therefore momentum, sensible and latent
516 heat transfer between the soil surface and the air flow, but also albedo and net radiation. Since
517 the aerodynamic resistance for mass and heat transfer in the free air flow decreases with
518 increasing surface roughness (see Figure 2 P1), the surface temperature of a rough evaporating
519 surface is lower than that of a smooth surface. For the silt soil, the difference is up to 2 °C
520 (Figure 18), which was rather small compared with the difference in surface temperature

521 between the two soils due to differences in evaporation resulting from differences in hydraulic
522 soil properties. A similar conclusion was drawn by *Dimitrov et al.* [2015] who compared surface
523 temperatures of plots with different surface roughness and found only small temperature
524 differences during stage I evaporation.

525

526 **Sensitivity of simulated evaporation on the parameterization of vapor**
527 **transport.**

528 In the previous examples, vapor transport in the soil was assumed to occur only due to diffusion.

529 An enhancement factor η was used to account for an increase in vapor transport due to a thermal
530 gradient, which may be larger in the air phase than in the bulk soil due to local thermal non-
531 equilibria. In order to investigate the relevance of the enhancement factor and turbulent
532 diffusivity within the porous medium on simulated evaporation fluxes, we considered four
533 cases: (i) reference with an enhancement factor η , (ii) no enhancement factor, (iii) an
534 enhancement factor together with an augmented diffusion coefficient by a factor 10 to represent
535 turbulent diffusion with, and (iv) no enhancement factor, but an augmented diffusion coefficient
536 by a factor 10 to represent turbulent diffusion.

537 In Figure 19, the simulated evaporation fluxes for the different cases in the sandy loam soil are
538 shown and in Figure 20, depth profiles of the simulated liquid and isothermal and thermal vapor
539 fluxes at DOY 235.5. Around midday, a strong positive temperature gradient existed at the soil
540 surface, which led to a downward thermal vapor flux. This downward thermal vapor flux was
541 enhanced by the enhancement factor and compensated the upward isothermal vapor flux from
542 the wetter subsoil towards the dry soil surface (Figure 20). The enhancement factor therefore
543 tended to reduce the net vapor fluxes during the day when radiation is the highest. For the case
544 with an enhancement factor and a diffusion coefficient that is a factor 10 higher, the thermal
545 vapor fluxes compensated the isothermal vapor fluxes completely. In this case, the highest
546 evaporation fluxes were simulated during the morning and evening when the thermal gradients

547 near the soil surface were small (Figure 19). Whether this simulated temporal evolution of the
548 evaporation rate is realistic is questionable. When no enhancement factor was used, the vapor
549 flux followed more closely the diurnal radiation dynamics and cumulative vapor losses were
550 larger. Based on daily evaporation losses, it is difficult to discriminate the effect of enhanced
551 vapor transport from the effect of soil hydraulic properties. Monitoring the dynamics of bare
552 soil evaporation, e.g. using eddy covariance measurements, Bowen ratios or high precision
553 lysimetry, seems to be promising to elucidate the impact or relevance of enhancement factors
554 for vapor transport. Data of hourly evaporation rates measured in lysimeters (e.g. [Novak, 2010;
555 Tolk et al., 2015; Van Bavel and Reginato, 1965; Yang et al., 2014]) or at higher temporal
556 resolutions measured with eddy covariance indicate that also during stage II, evaporation rates
557 follow the diurnal dynamics of the radiation, which indicates that enhancement factors for non-
558 isothermal vapor transport may be less important.

559

560 **Parameterization of transfer resistances for a semi-coupling of the** 561 **Richards equation with evaporative forcing.**

562 The semi-coupled approach should be able to reproduce diurnal evaporation dynamics. To
563 evaluate this approach, we derived β factors (ratio of the aerodynamic resistance to the sum of
564 the soil surface and aerodynamic resistance) from evaporation rates and soil moisture contents
565 of the top layer at midday that were simulated using the coupled non-isothermal vapor-water
566 flow model (Figure 21). A problem with the semi-coupled approach is that the thickness of the
567 soil surface layer is not defined. Therefore, we calculated average moisture contents in surface
568 layers of 0.4, 1 and 2 cm thickness and plotted the β factors versus these averaged water
569 contents.

570 The simulation results indicated a strong dependence of the β factor on the chosen thickness of
571 the soil surface layer. When the soil surface layer is thin and the evaporation front sinks below
572 the bottom of the surface layer, the β factor becomes independent of the water content in the

573 surface layer. Another problem with this approach is that the effect of temperature and
574 temperature gradients on the soil surface resistance term is not considered. We calculated β
575 factors from simulations using the reference enhancement factor, η , and simulations that do not
576 use an enhancement factor. For the latter simulations, the impact of downward thermal
577 gradients on the evaporation flux was much smaller so that for the same water content in the
578 surface layer, a higher evaporation flux (higher β) was obtained. Difference in β factors
579 obtained from these simulations demonstrate the sensitivity of the β factors to not well
580 characterized processes such as enhancement of fluxes due to temperature gradients. Finally,
581 the scatter of the relation between β and θ for a certain enhancement factor and layer thickness
582 could be related to the differences in temperature in the surface layer with higher temperatures
583 leading to a positive deviation and lower temperatures to a negative deviation.

584

585 **Conclusions**

586 Lateral variations in soil properties, water infiltration, and/or radiation lead to lateral variations
587 in state variables and fluxes. At the soil surface these variations are coupled to transfer processes
588 in the free flow and the soil. When the soil surface is sufficiently wet, the evaporation does not
589 depend on the local hydraulic properties of the soil and their spatial variability.

590 The evaporation rate from wet surfaces can be assumed to be nearly uniform and to vary little
591 in the main wind direction for sufficiently large and uniform areas with a sufficiently large
592 fetch. This uniform evaporation rate could be calculated using vertical gradients of air
593 temperature, air humidity, and wind speed in the free flow, net radiation on the porous medium
594 surface and a surface energy balance.

595 The potential evaporation could be used as a uniform boundary condition for a 3-D flow model
596 in a heterogeneous wet porous medium and could serve as boundary condition for upscaling

597 heterogeneous flow in the vadose zone [Li *et al.*, 2015]. However, problems arise when parts
598 of the heterogeneous surface dry out so that the evaporation flux from these parts decreases. A
599 commonly used approach to simulate such cases is to use a threshold boundary condition as
600 used in 1-D models [Schlüter *et al.*, 2012] or to use 1-D aerodynamic transfer resistances that
601 depend on the soil water content. However, such approaches do not account for an increase in
602 evaporation from wet parts of the heterogeneous surface that arise from lateral variations in free
603 flow variables (air humidity and air temperature) due to variations in evaporation and
604 evaporative cooling on the soil surface [Bechtold *et al.*, 2012]. Also, lateral heat fluxes within
605 the soil can contribute to an enhanced evaporation from wet soil patches [Shahraeeni and Or,
606 2011]. Our simulation studies demonstrated that lateral heat fluxes in the soil play an important
607 role and neglecting them leads to an underestimation of the evaporation rate from wet patches.
608 It should be noted that in our simulations, we did not consider radiation. We expect that
609 radiation will increase the importance of lateral heat fluxes.

610 Models that couple free flow with processes in the porous medium can be used to simulate
611 compensatory evaporation from wet patches on a heterogeneous surface. However, such
612 simulations are computationally expensive. Therefore, correction factors, which depend on free
613 flow conditions, porous medium properties, and the spatial scale and geometry of wet patches,
614 to adjust evaporation from wet patches that can be used as boundary conditions in porous media
615 models could be of practical importance. It should be noted that such correction factors have
616 already been derived to estimate, for instance, the effect of the size of evaporation pans, ponds,
617 or lakes on the evaporation from these surfaces. However, these factors do not account for
618 lateral heat and water flow within the porous medium.

619 For large fetches, when lateral variations in state variables and vertical fluxes in the free flow
620 and the porous medium can be neglected, one-dimensional modelling approaches can be used.
621 The main differences between these models are the description of vapor fluxes in the porous
622 medium and the coupling between heat and water balances. The Richards equation, which

623 neglects vapor fluxes and which is not coupled to a heat flow equation in the porous medium,
624 simulated similar cumulative evaporation as the more comprehensive model that includes vapor
625 transport in the porous medium. The effect of neglecting vapor transport in the porous medium
626 and the choice of the threshold boundary pressure head, ψ_{crit} , on simulated cumulative
627 evaporation fluxes could be evaluated using the desorptivity, which is an integral function of
628 the hydraulic conductivity. When vapor transport in the porous medium was more important
629 than liquid flow, the diurnal dynamics of evaporation could not be reproduced by the Richards
630 equation using a threshold boundary condition, which decouples evaporation dynamics from
631 the dynamics of evaporative forcing during stage II evaporation. However, a boundary
632 condition for the Richards equation that combines the diurnal dynamics of the evaporation of a
633 wet surface (evaporative forcing) with a soil surface resistance depending on the soil water
634 content could be used to reproduce the diurnal evaporation dynamics. In this so-called semi-
635 coupled approach, which is often used in large scale simulation models, the heat fluxes in the
636 porous medium are not considered and heat and water balances are only coupled at the porous
637 medium free flow interface. The parameterization of this soil resistance term depends on the
638 thickness of the considered soil surface layer and on the effect of temperature and temperature
639 gradients on evaporation. The latter indicates that this resistance term should depend on the
640 climatic conditions.

641 Vapor transport and its parameterization representing processes like turbulent pumping and
642 thermal non-equilibrium mainly affect the diurnal dynamics of evaporation. Monitoring the
643 diurnal dynamics of evaporation therefore provides indirect information about processes
644 controlling vapor transport in porous media and could be useful to parameterize non-equilibria
645 processes.

646 Neglecting vapor transport in the Richards equation and decoupling heat and water fluxes in
647 the porous medium also has an impact on the predicted soil moisture and temperature profiles
648 close to the soil surface. Due to the monotonous increase of the water diffusivity with increasing

649 water content when vapor transport is not considered, Richards' equation cannot predict
650 'hooked' water content profiles that develop when the evaporation front recedes within the
651 porous medium. Since vapor transport in the porous medium is not considered, the Richards
652 equation assumes that the evaporation takes places at the soil surface. Therefore, it cannot
653 simulate the development of an evaporation front that recedes in the porous medium neither the
654 effect of this front on the temperature profile nor the surface temperature. Derivation of
655 evaporation rates from remotely sensed surface temperature data or detailed measurements of
656 temperature profiles therefore requires models that couple heat, water and vapor transport in
657 the soil.

658

659 **Acknowledgements:**

660

661 The authors would like to acknowledge the German Science Foundation, DFG. This work is a
662 contribution of the DFG research unit “Multi-Scale Interfaces in Unsaturated Soil” (MUSIS;
663 FOR 1083) and the DFG International Research Training Group NUPUS and the National
664 Science Foundation (NSF EAR-1447533).

665 The DuMu^x source code, the modified Hydrus source code, and the input files necessary to
666 reproduce the simulations are available from the authors upon request. The DuMux simulations
667 are available via <https://git.iws.uni-stuttgart.de/dumux-pub/Vanderborght2015a>. The authors
668 would like to thank the editor and the anonymous reviewers for their insightful comments and
669 suggestions that have contributed to improve this paper.

670

671 **Tables:**

672 **Table 1: Parameters of the Mualem van Genuchten hydraulic functions [van Genuchten, 1980] for two**
673 **different soils.**

texture	θ_r	θ_s	α [cm ⁻¹]	n	K_s [cm d ⁻¹]	l
silt	0.02	0.35	0.0042	1.324	91.2	0.5
sandy loam	0.065	0.41	0.08	1.65	106.1	0.5

674

675

676
677
678
679
680

Table 2: Average vapor concentration (ρ_g^w), temperature (T), and evaporation flux, F_w , at the surface of the upstream and downstream part of the homogeneous/heterogeneous porous medium setup (Figure 4) after 3 days of evaporation (Figure 5), 1-D aerodynamic resistances, r_v , for the upstream and downstream parts that are derived from evaporation rates and vapor concentrations in the homogeneous setup after 3 days of evaporation, and calculated fluxes using the 1-D aerodynamic resistances, r_v .

	Upstream part	Downstream part	Incoming air
	Silt	Silt	
ρ_g^w (kg m ⁻³)	9.33 10 ⁻³	9.12 10 ⁻³	6.52 10 ⁻³
T (°K)	283.12	282.73	293
F_w , (FC)* (kg m ⁻² s ⁻¹)	4.81 10 ⁻⁵	2.64 10 ⁻⁵	
r_v (s m ⁻¹)	58,4	98,5	
	Silt	Sand	
ρ_g^w (kg m ⁻³)	9.56 10 ⁻³	8.45 10 ⁻³	
T (°K)	283.43	284.32	
F_w (FC) (kg m ⁻² s ⁻¹)	5.28 10 ⁻⁵	1.27 10 ⁻⁵	
F_w (1D) (kg m ⁻² s ⁻¹)	5.20 10 ⁻⁵	1.96 10 ⁻⁵	
	Sand	Silt	
ρ_g^w (kg m ⁻³)	7.62 10 ⁻³	9.64 10 ⁻³	
T (°K)	286.97	283.55	
F_w (FC) (kg m ⁻² s ⁻¹)	1.87 10 ⁻⁵	4.16 10 ⁻⁵	
F_w (1D) (kg m ⁻² s ⁻¹)	1.88 10 ⁻⁵	3.17 10 ⁻⁵	
F_w (1D) (kg m ⁻² s ⁻¹)**		5.34 10 ⁻⁵	

681 * FC fully coupled

682 ** The aerodynamic resistance of the upstream part is used to calculate the evaporation from
683 the downstream part. It is assumed that the mass transfer boundary layer is equal to the one
684 above the upstream part when the upstream part does not evaporate anymore.

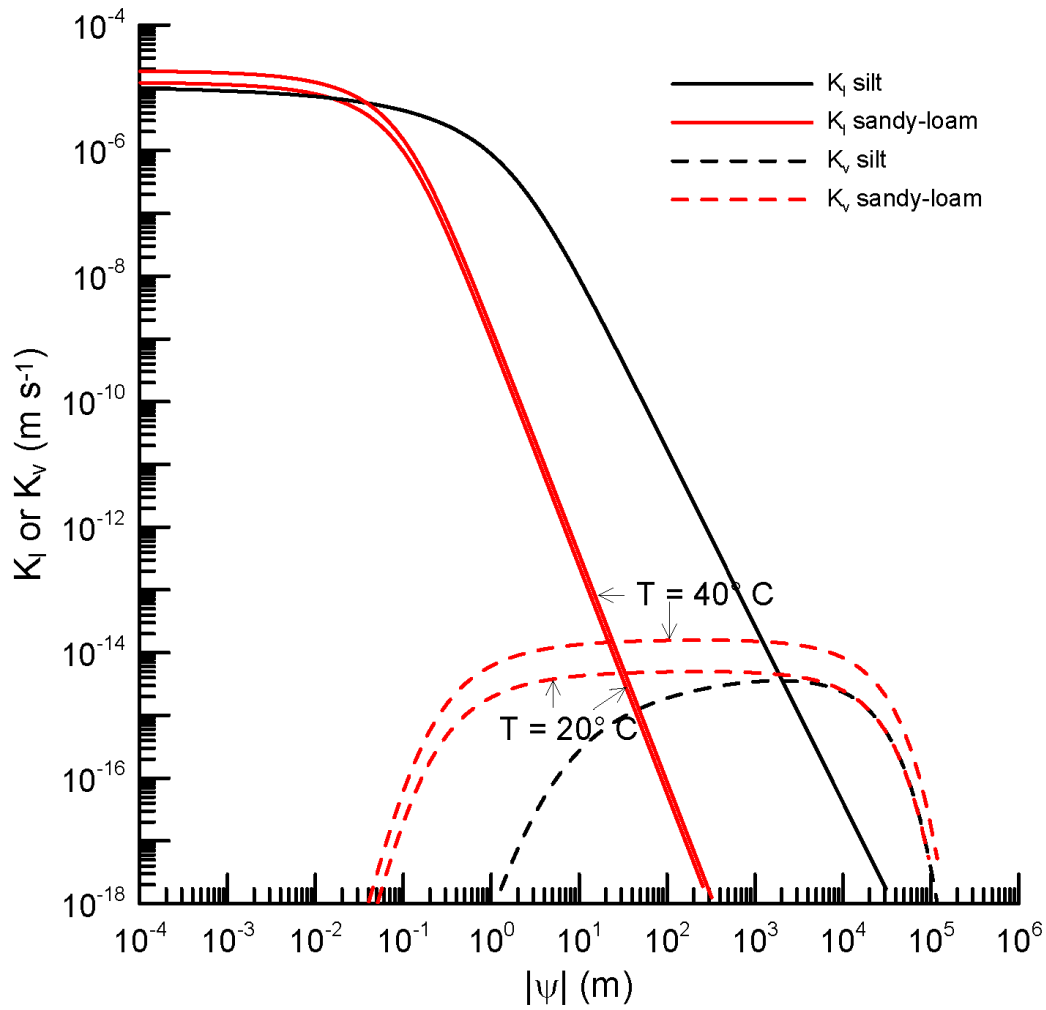
685 **Table 3: Initial, ψ_i , and surface, ψ_{sur} , pressure head, S_{evap} calculated from Eq. [8], from Eq. [8] with $K_{v\psi}=0$,**
686 **for two different threshold pressure heads : $\psi_{sur} = \psi_{crit}$, and S_{evap} fitted to the simulated cumulative**
687 **evaporation using Eq. [7] for the two different soils. The cumulative evaporation amounts during stage II,**
688 **E_{cum} , that are simulated by the non-isothermal vapor-water flow model and by the Richards model for two**
689 **different ψ_{crit} 's are given for the corresponding S_{evap} values.**

texture	ψ_i	ψ_{sur}	S_{evap}	S_{evap} ($K_{v\psi} = 0$)	S_{evap} ($\psi_{sur} = -10^5$ cm)	S_{evap} ($\psi_{sur} = -10^4$ cm)	S_{evap} fit
	cm		cm d ^{-0.5}				
silt	- 2.3 10 ³	- 2.6 10 ⁶	0.84	0.83	0.82	0.72	0.83
			E_{cum} stage II (cm)				
			1.82		1.86	1.57	
sandy loam	-5.0 10 ¹	-3.6 10 ⁶	0.39	0.36	0.36	0.36	0.30
			E_{cum} stage II (cm)				
			0.77		0.73	0.73	

690

691

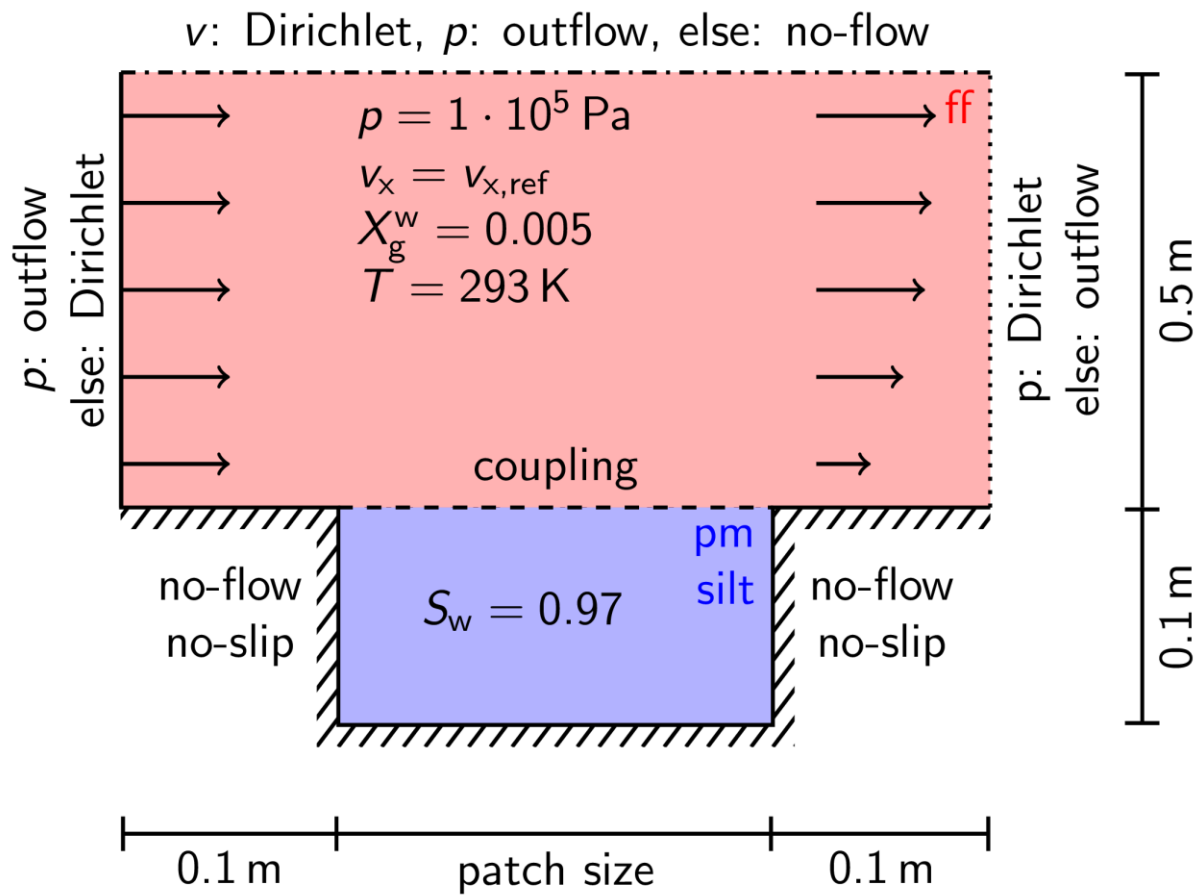
692 **Figures:**



693

694 **Figure 1: Isothermal hydraulic conductivity of the liquid ($K_{l,\psi}$ solid lines) and vapor phase ($K_{v,\psi}$, dashed**
 695 **lines) at 20°C as a function of the absolute value of the water pressure head, ψ , for the sandy loam and silty**
 696 **soil (see Table 1) and isothermal conditions. For the sandy loam soil, also conductivities at 40°C are shown.**

697



698

699 **Figure 2: Setup for evaporation from a soil sample with different lengths /patch sizes: 0.1 m, 0.2 m, 0.5 m,**

700 **1.0 m, and 2.0 m. Air is flowing from left to right with different wind speeds $v_{x,ref}$: 0.5 m s⁻¹, 1.0 m s⁻¹, and**

701 **5.0 m s⁻¹. The discretization is equidistant in the horizontal direction ($\Delta x = 0.02$ m), in the vertical direction**

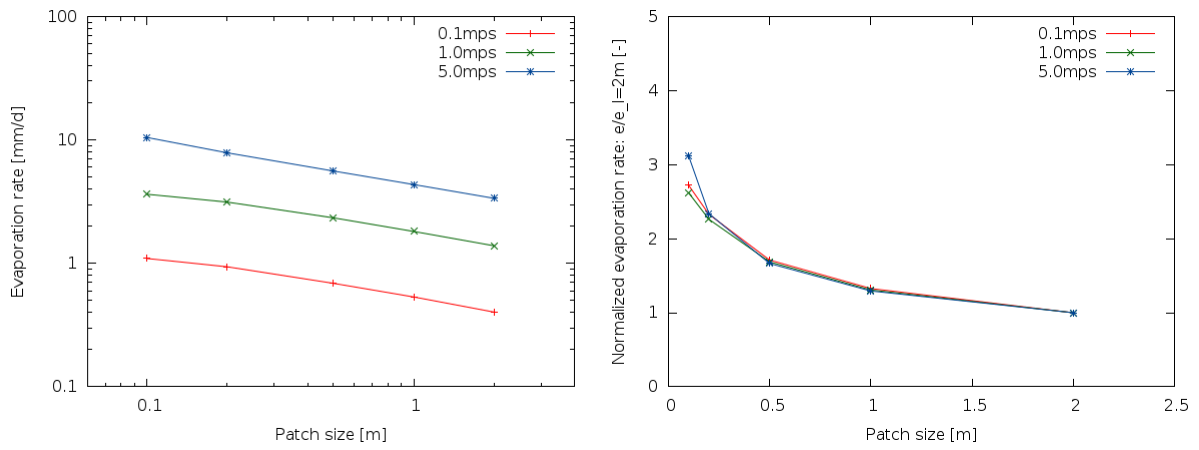
702 **20 cells are located in the free flow and 10 in the porous medium, both with a grading towards the interface.**

703

704

705

706

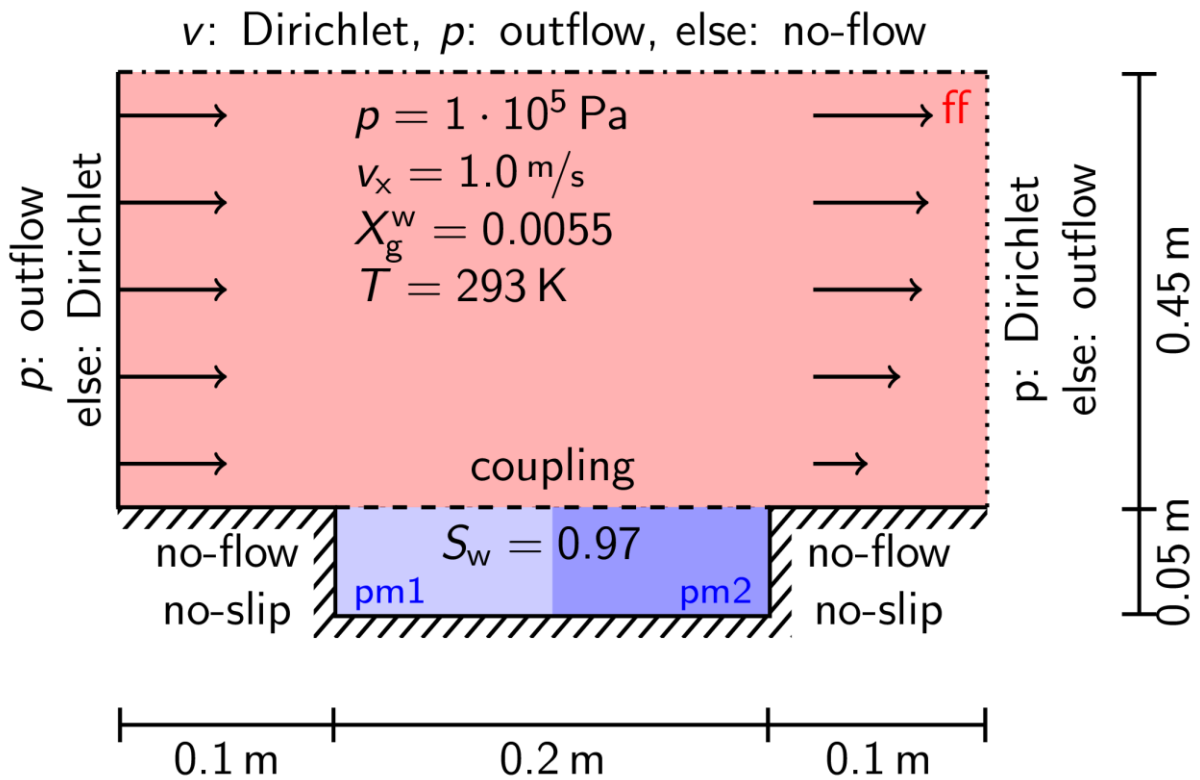


707

708

709 **Figure 3: Simulated stage-I steady-state evaporation rates from wet silt soil patches with different patch**
710 **sizes, using the fully turbulent model. The normalized evaporation rate is the evaporation rate divided by**
711 **the evaporation rate obtained from the maximum patch size (2 m).**

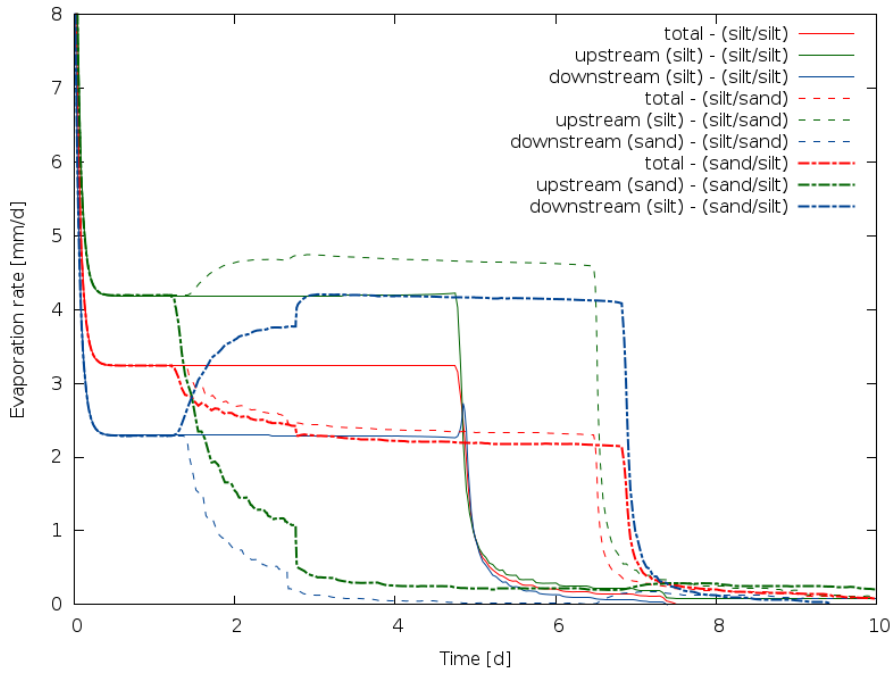
712



714

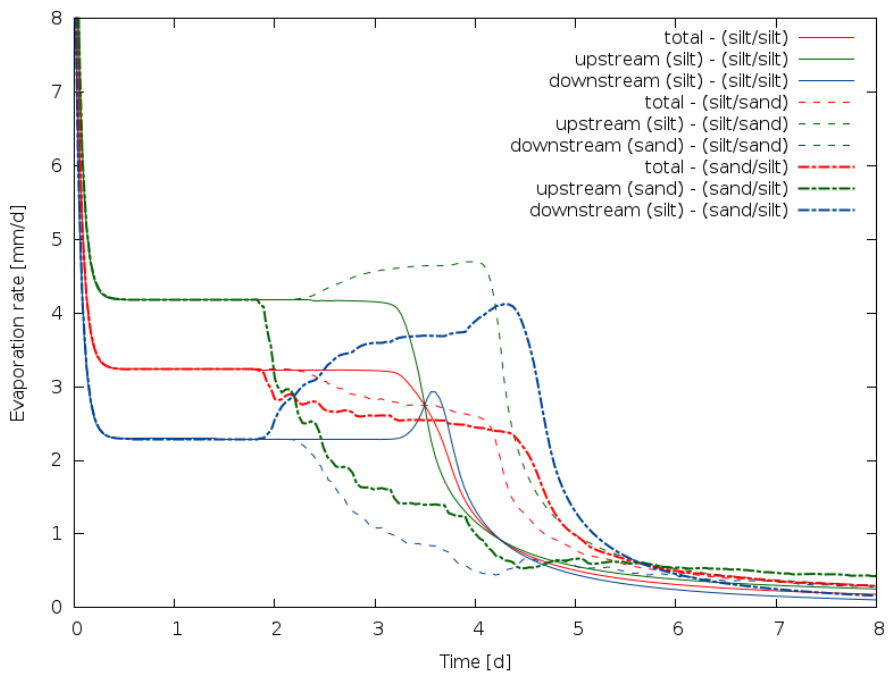
715 **Figure 4: Setup for evaporation from a homogeneous/heterogeneous soil sample. In the homogeneous case,**
 716 **the porous medium is filled with silt, in the heterogeneous case one part is filled with silt and the other with**
 717 **sandy loam. Air is flowing from left to right, the porous medium is fully isolated. The problem discretized**
 718 **using 41 cells in horizontal and 40 cells in vertical direction (25 in the free flow and 15 in the porous medium)**
 719 **with a grading towards the interface.**

720



721

OLD

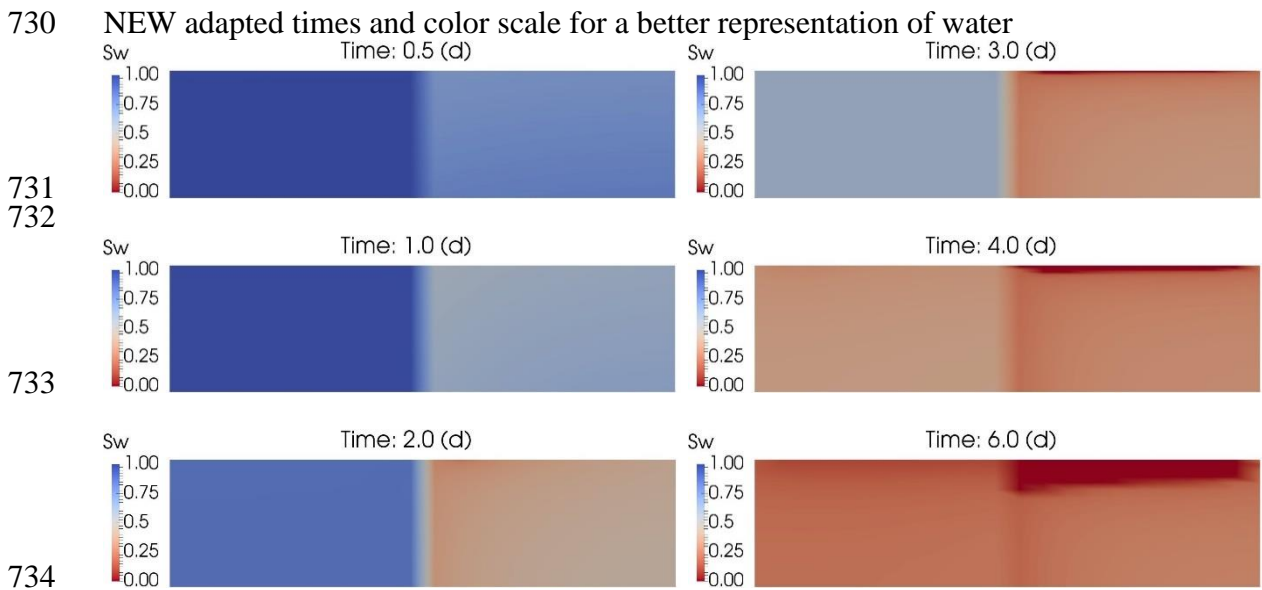


722

NEW changed x-scale

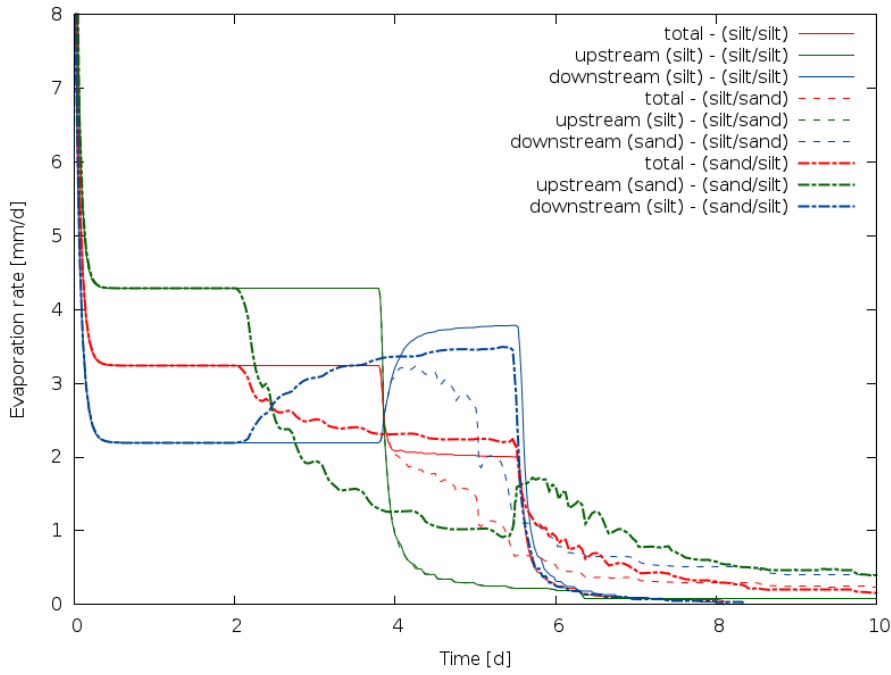
723 **Figure 5: Evaporation rates from a homogeneous soil and a soil with heterogeneity in the horizontal**
 724 **direction (see Figure 4). Red lines represent average evaporation rates from the entire simulation domain,**
 725 **green lines from the upstream part and blue lines from the downstream. Full lines are evaporation rates for**
 726 **the homogeneous case (both parts are filled with silt), dashed lines for the case that the upstream part is**
 727 **filled with silt and the downstream part with sandy loam, and dashed dotted lines for the upstream part**
 728 **filled with sandy loam and the downstream part with silt.**

729



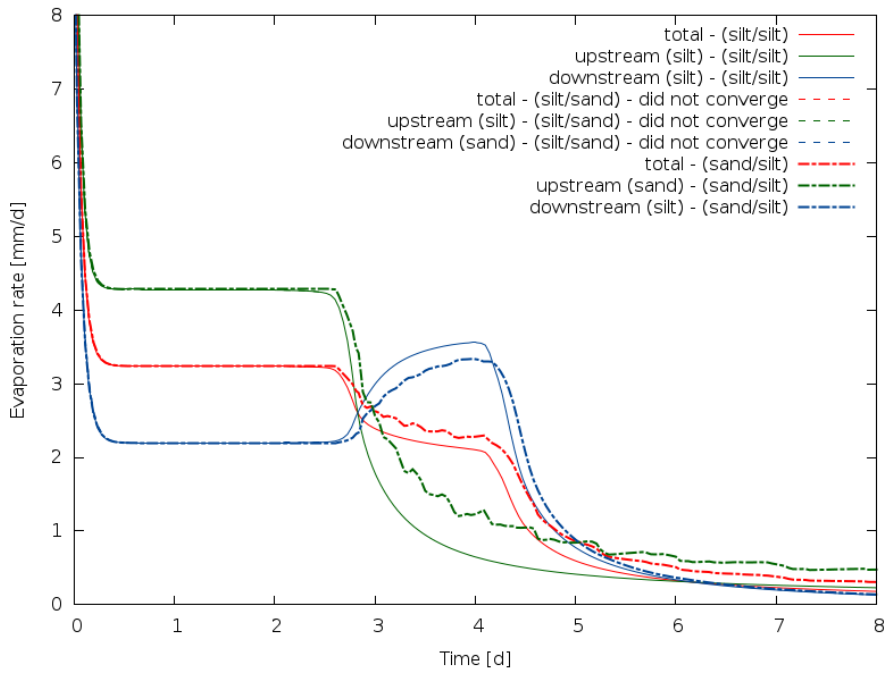
736 **Figure 6: Drying process for heterogeneous porous medium over time (see Figure 4 for setup). The water**
 737 **saturation (S_w) distribution in the porous medium is shown at six different times. The left/upstream half of**
 738 **the domain is silt, the right/downstream half is sandy loam.**

739



740

OLD



741

NEW changed x-scale

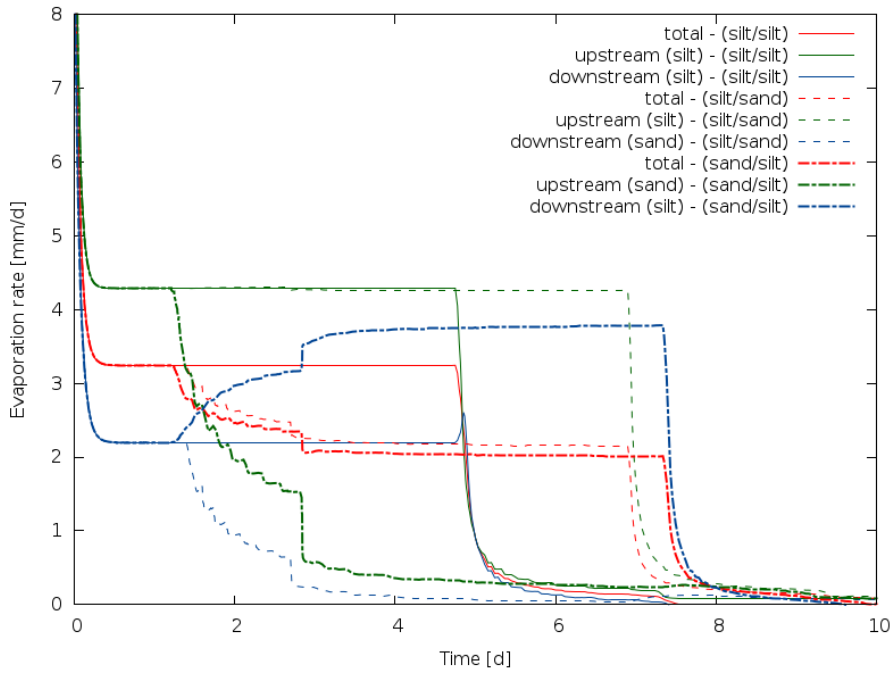
742

Figure 7: Evaporation rates for the same setup as shown in Figure 4 and Figure 5 but for the case that exchange of heat and water across the vertical interface between the upstream and downstream parts of the domain were disabled.

743

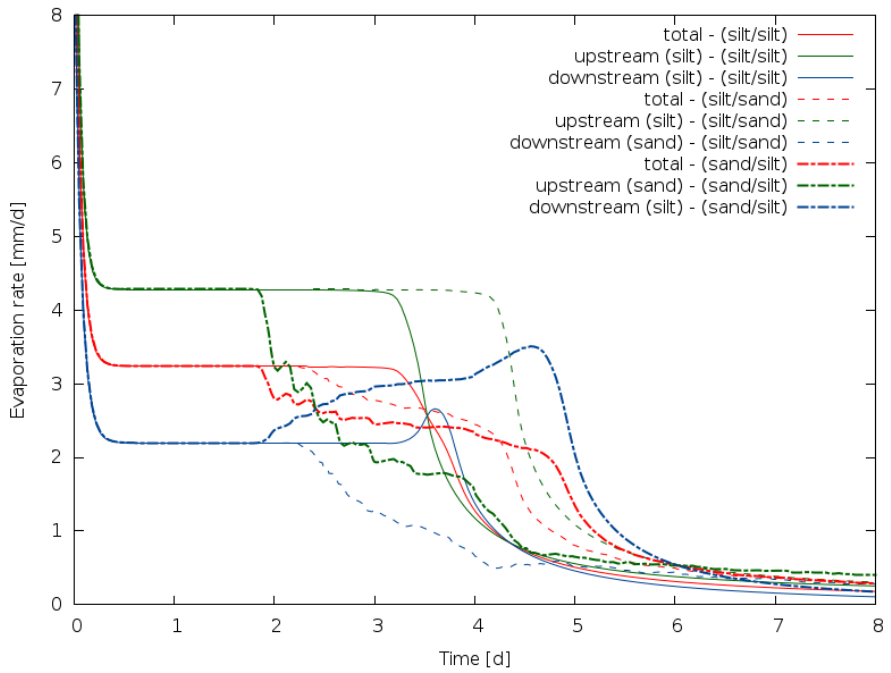
744

745



746

OLD



747

NEW changed x-scale

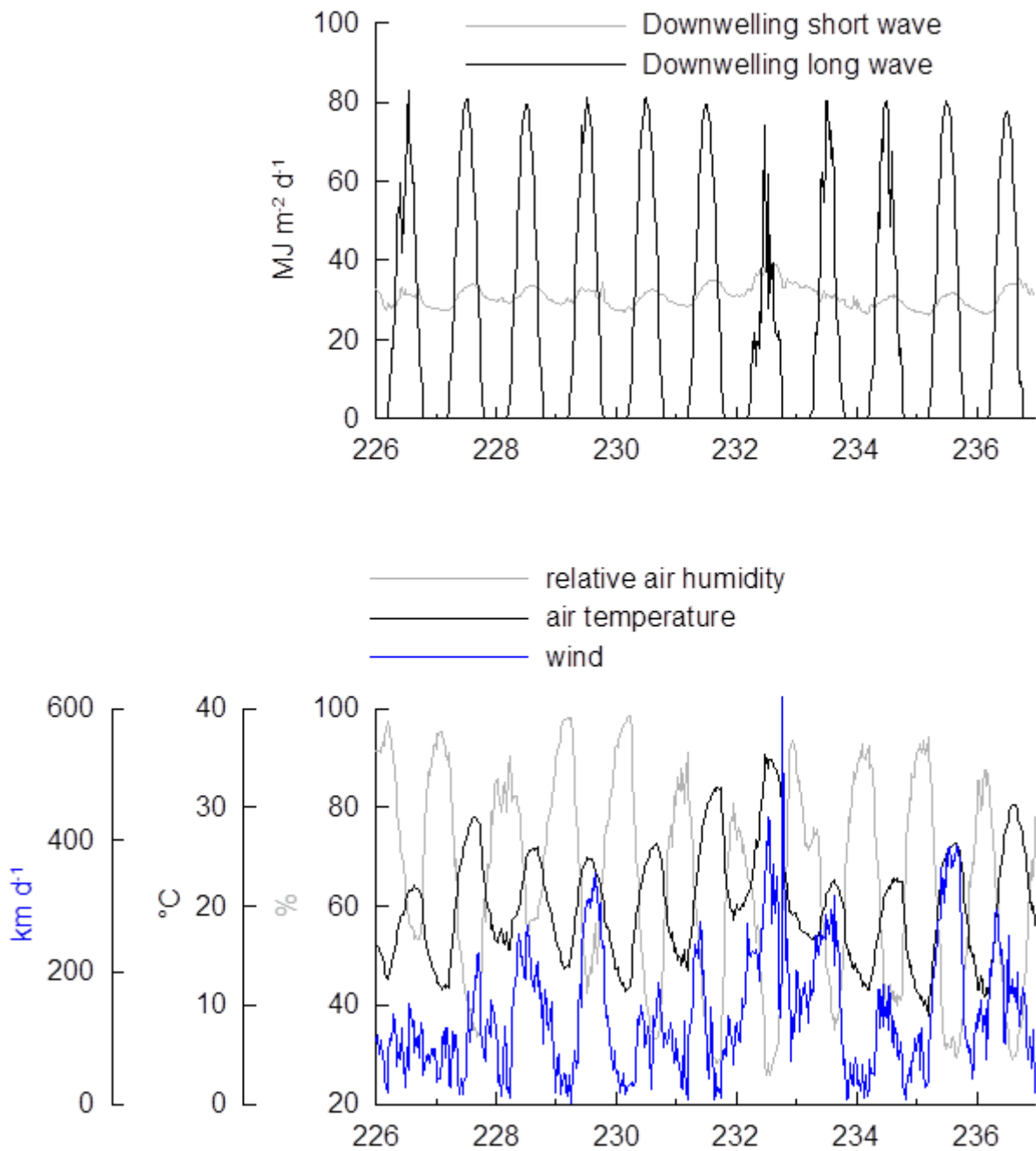
748

Figure 8: Evaporation rates for the same setup as shown in Figure 4 and Figure 5 but for the case that
conductive heat fluxes across the vertical interface between the upstream and downstream parts of the
domain were disabled.

750

751

752



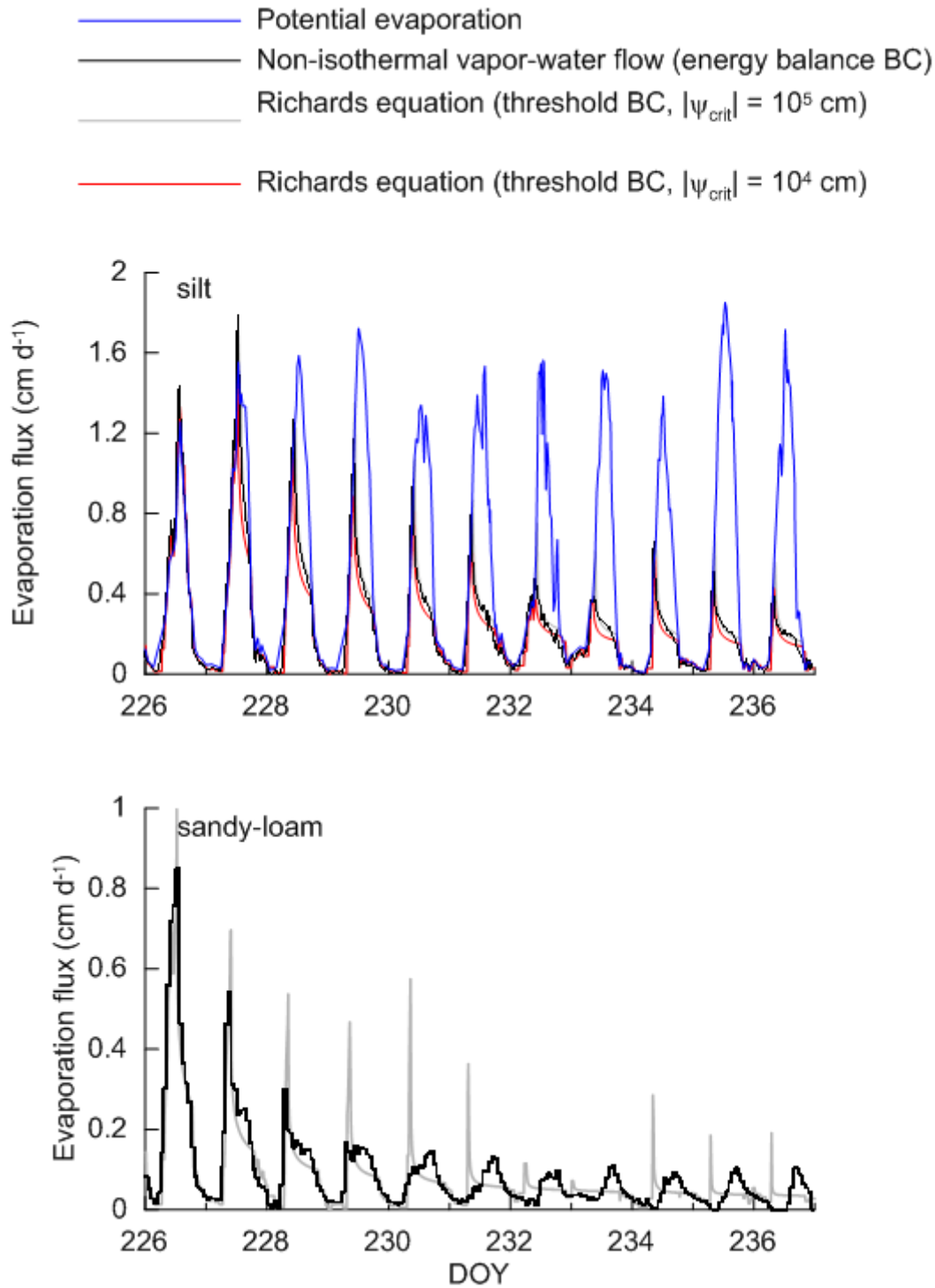
753

754 **Figure 9: Time series of downwelling short and long wave radiation (top) and wind speed, air temperature**

755 **and air humidity at 1.45 m height (bottom).**

756

757



758

759 **Figure 10: Time series of simulated evaporation rate from the silt soil (top) and sandy loam soil (bottom)**

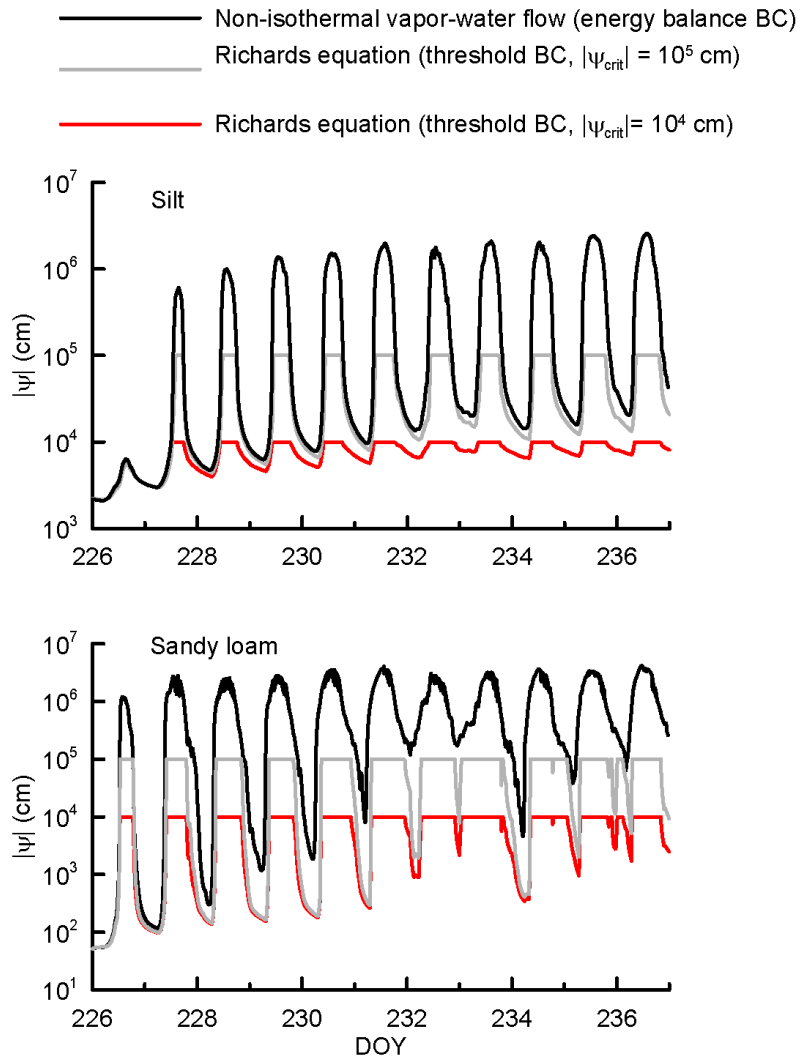
760 **using a model that considers non-isothermal vapor-water flow (black line) and using the Richards equation**

761 **with threshold boundary conditions for $\psi_{crit} = -10^4$ cm (red line) or $\psi_{crit} = -10^5$ cm (grey line). The blue line**

762 **represents the potential evaporation rate from a wet soil surface. Note the different scale of the y-axes for**

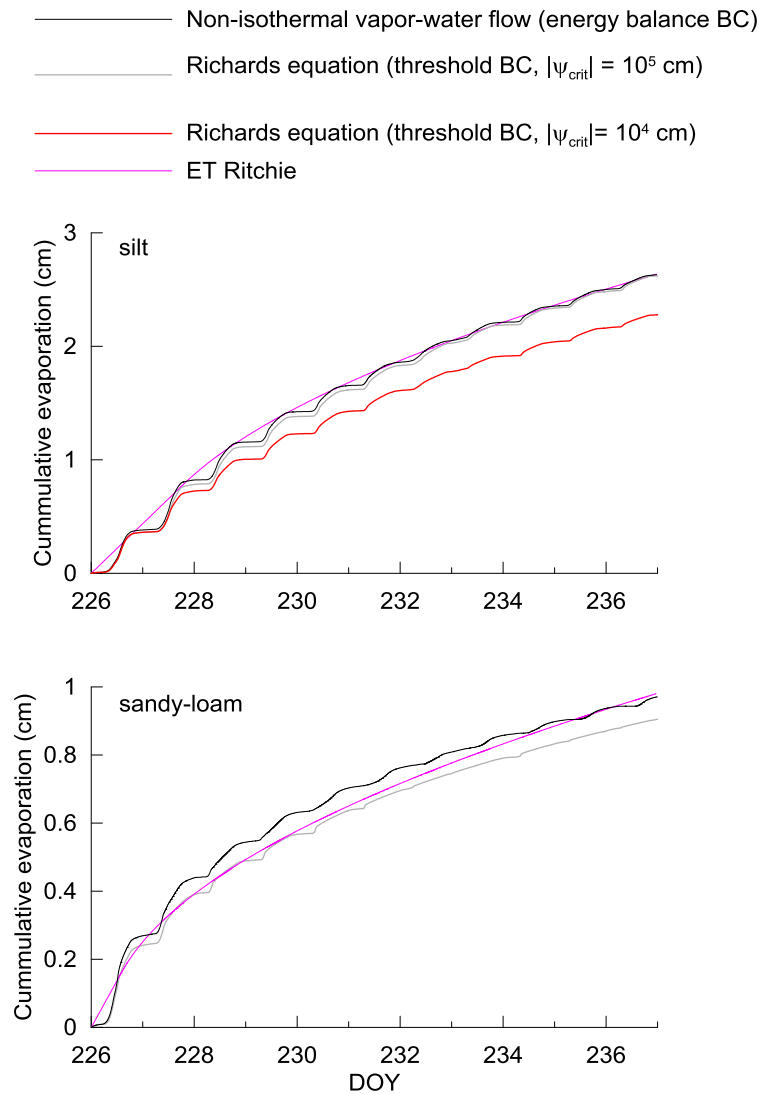
763 **the two plots. For the sandy loam, simulated evaporation using Richards equation overlapped for the two**

764 **boundary thresholds.**



766

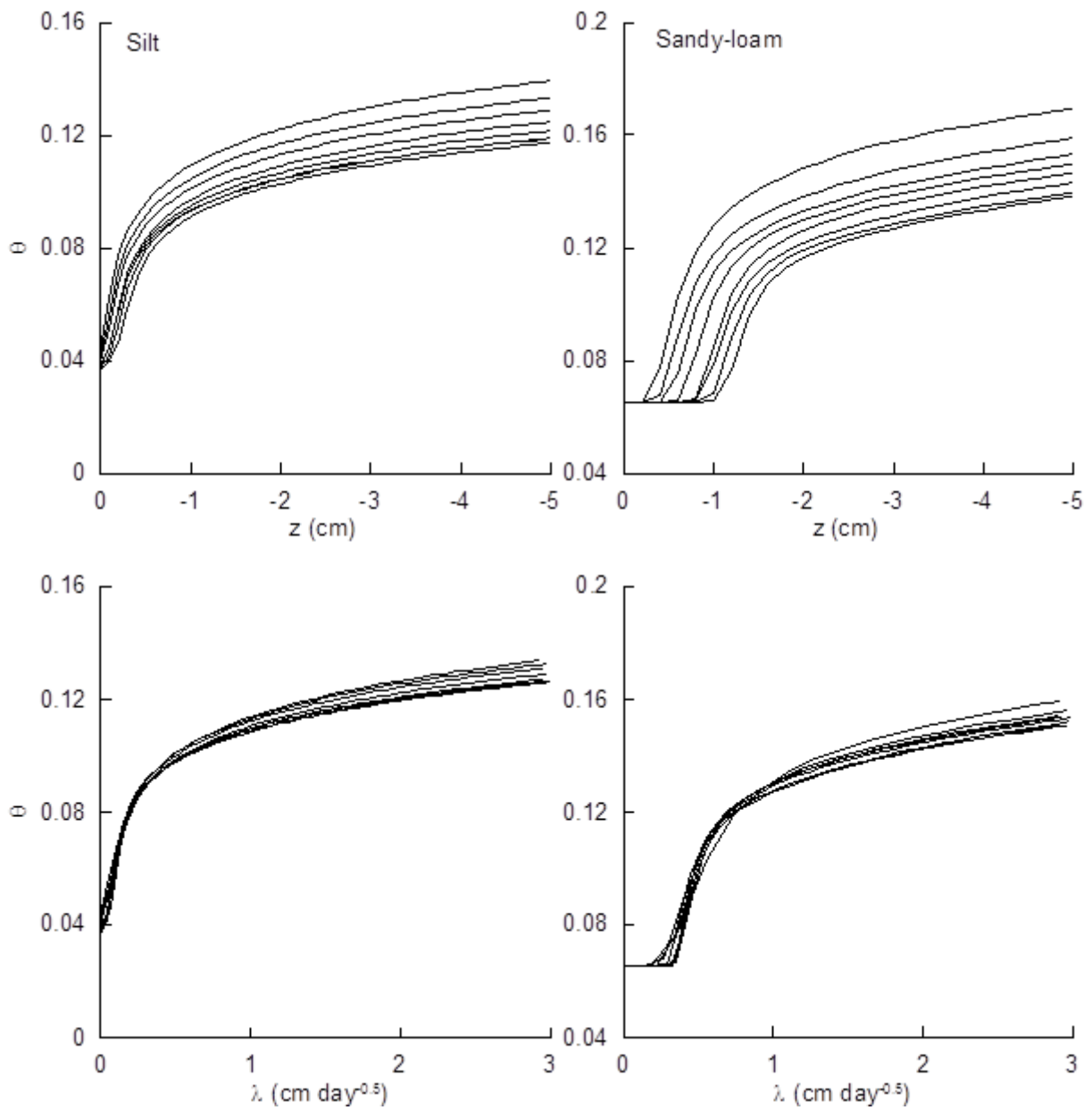
767 **Figure 11: Evolution of the absolute pressure head, $|\psi|$, that is simulated at the soil surface of the silt soil**
 768 **(top) and sandy loam soil (bottom) using a non-isothermal vapor-water flow model (black line) and Richards**
 769 **model with a threshold boundary condition for $\psi_{crit} = -10^4$ cm (red line) or for $\psi_{crit} = -10^5$ cm (grey line)**



771

772 **Figure 12: Cumulative evaporation in the silt soil (top) and sandy loam soil (bottom) simulated using the**
 773 **non-isothermal vapor-water flow model (black), the Richards model (Eq. [7]) with a threshold boundary**
 774 **condition $\psi_{crit} = -10^4$ cm (red line) or $\psi_{crit} = -10^5$ cm (grey line), and the Ritchie model (magenta). The**
 775 **cumulative potential evaporation for the considered period was 5.24 cm.**

776



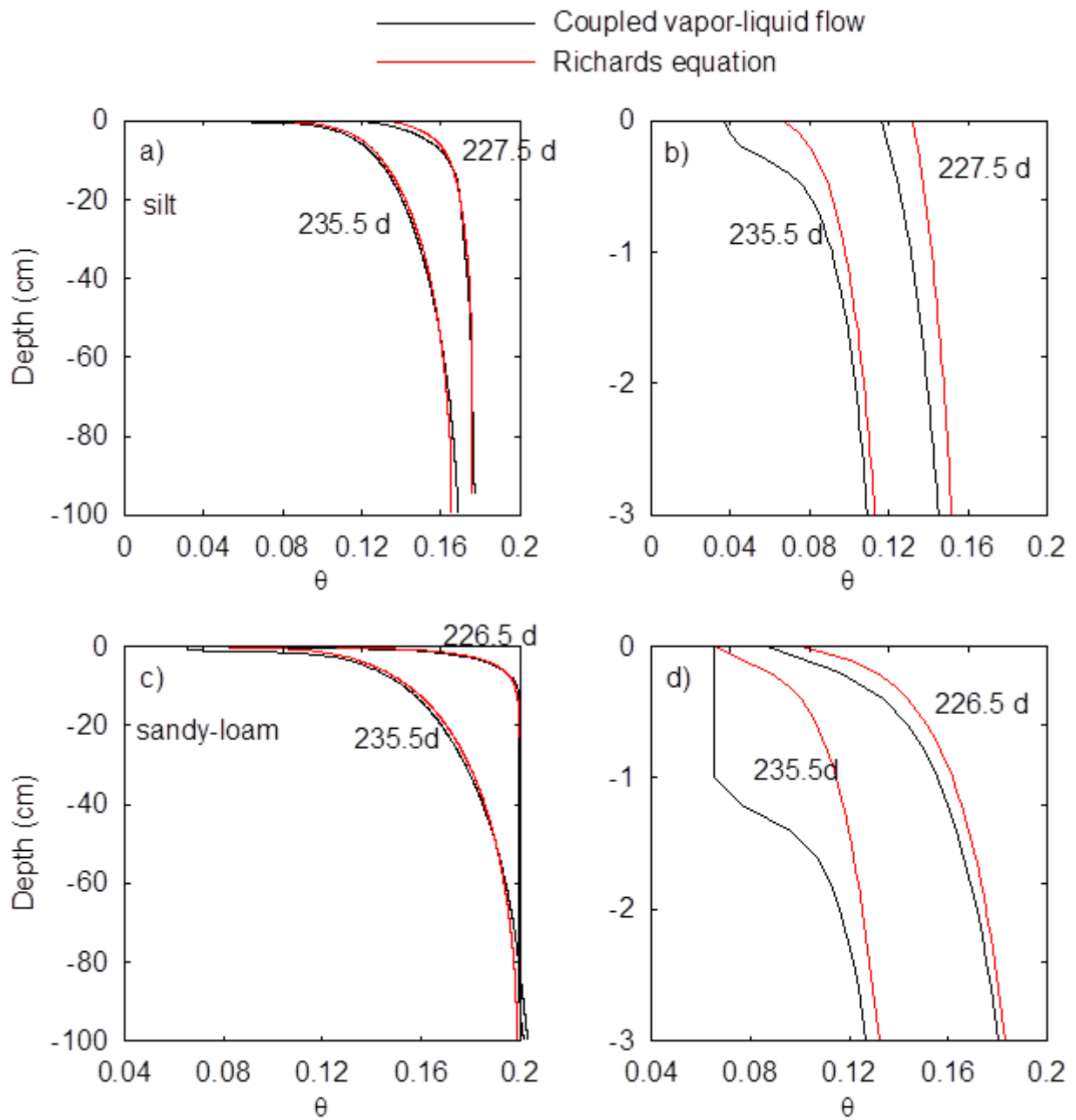
777

778 **Figure 13: Simulated soil moisture profiles at different times in the silty soil (left) and sandy loam soil (right)**

779 **plotted versus depth (top panels) and versus the scaled depth $\lambda = |z| t^{-0.5}$ (bottom panels).**

780

781



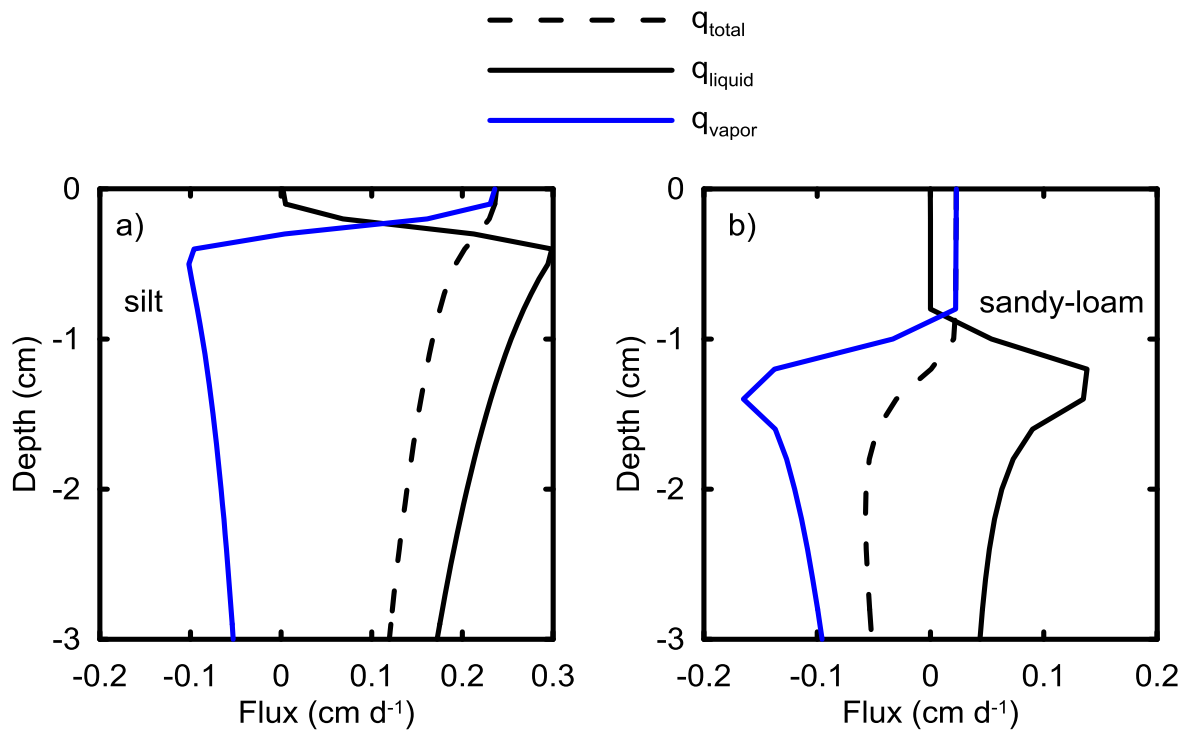
782

783 **Figure 14: Depth profiles of the water content simulated using a non-isothermal vapor-water flow model**

784 **(black line) and the Richards equation (red line) in the silt (top panels) and sandy loam (bottom panels) soil.**

785 **The right panels zoom in the top 3 cm of the soil profile.**

786



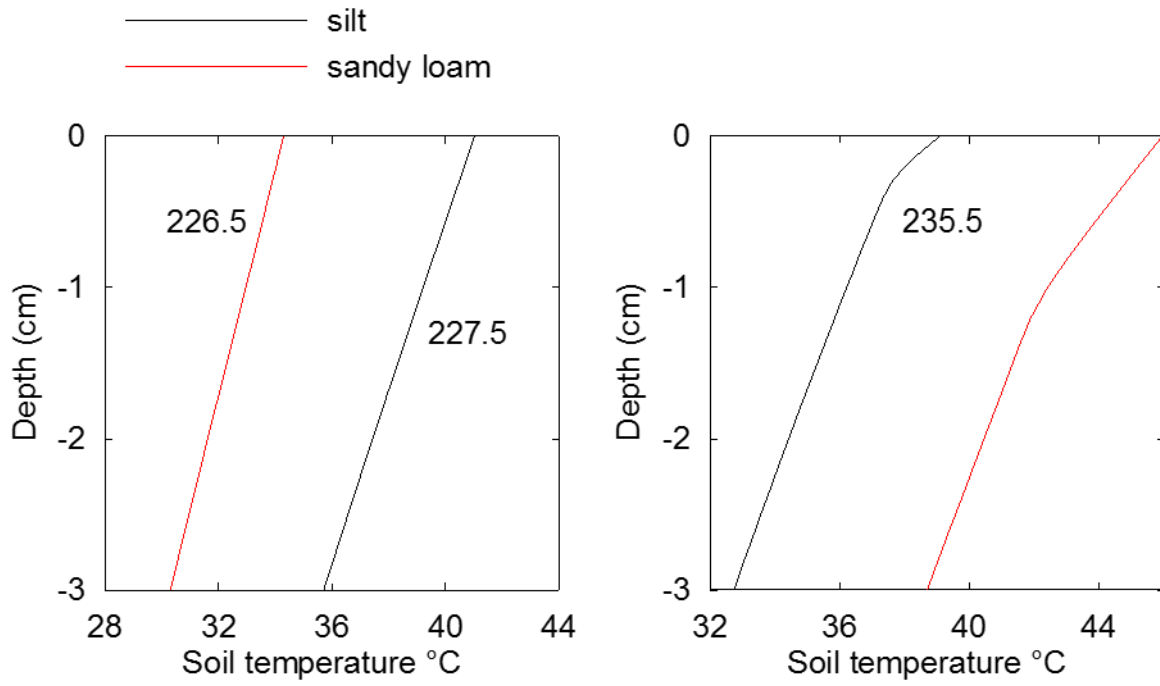
787

788

789 **Figure 15: Depth profiles of the total water flux (q_{total} , dashed black line), the liquid water flux (q_{liquid} , solid**
 790 **black line) and the vapor flux (blue line q_{vapor}) in the silt soil (left) and in the sandy loam soil (right) at DOY**
 791 **235.5. The Water fluxes are given in equivalent depths of liquid water.**

792

793



794

795

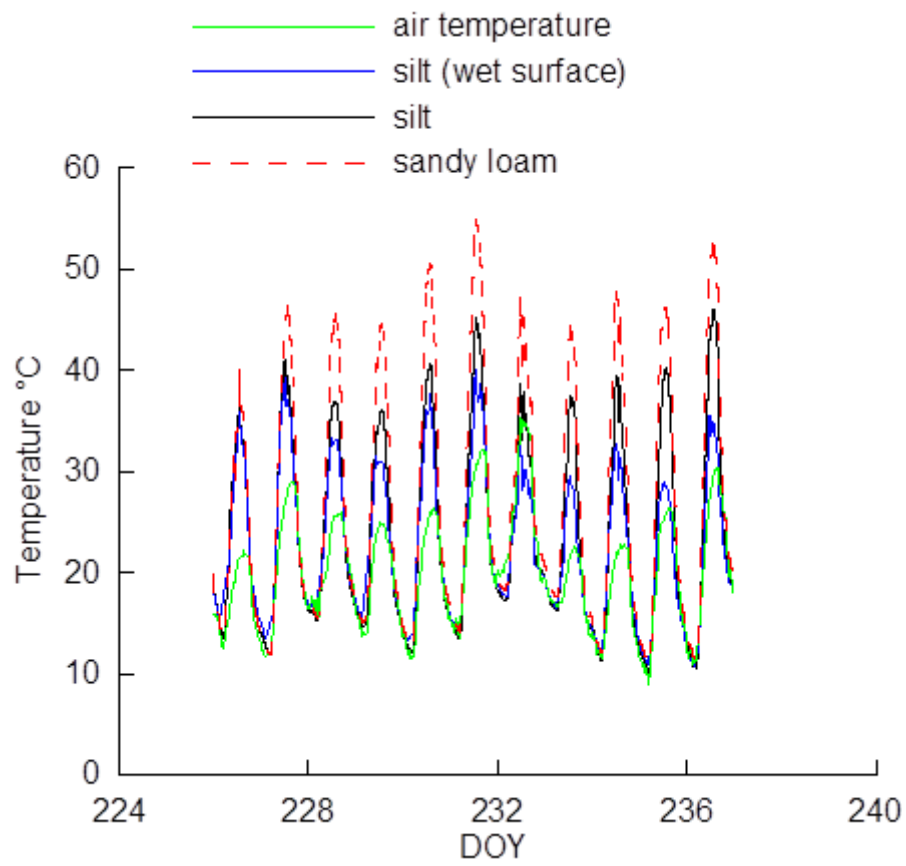
796 **Figure 16: Depth profiles of soil temperature at the beginning (left) and end (right) of the simulation period**

797 **in the silt (black line) and sandy loam soil (red line).**

798

799

800



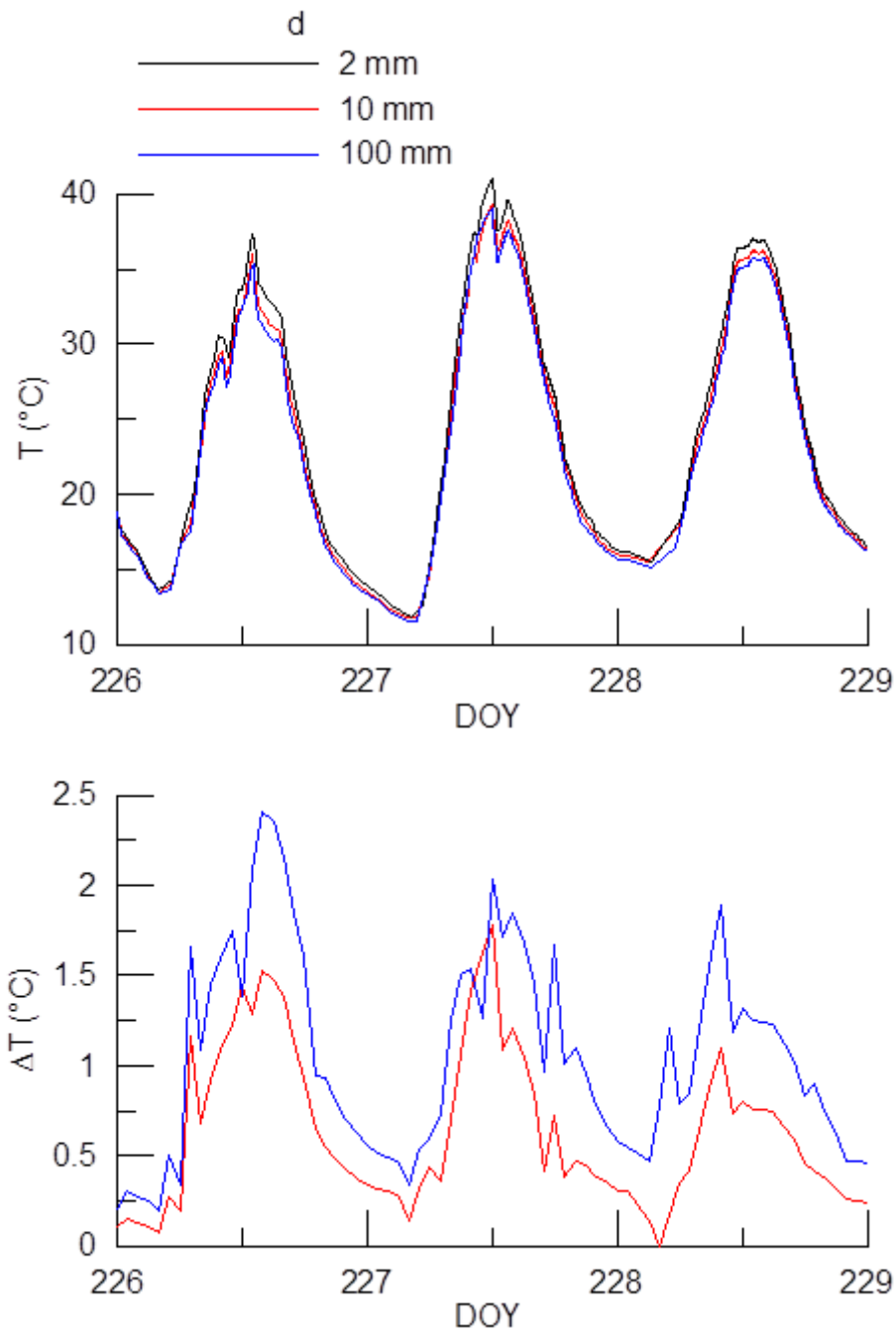
801

802 **Figure 17: Air temperature (green line) and simulated surface temperature of a silt soil (black), a sandy**
 803 **loam (dashed red), and a silt soil with a wet surface (blue).**

804

805

806



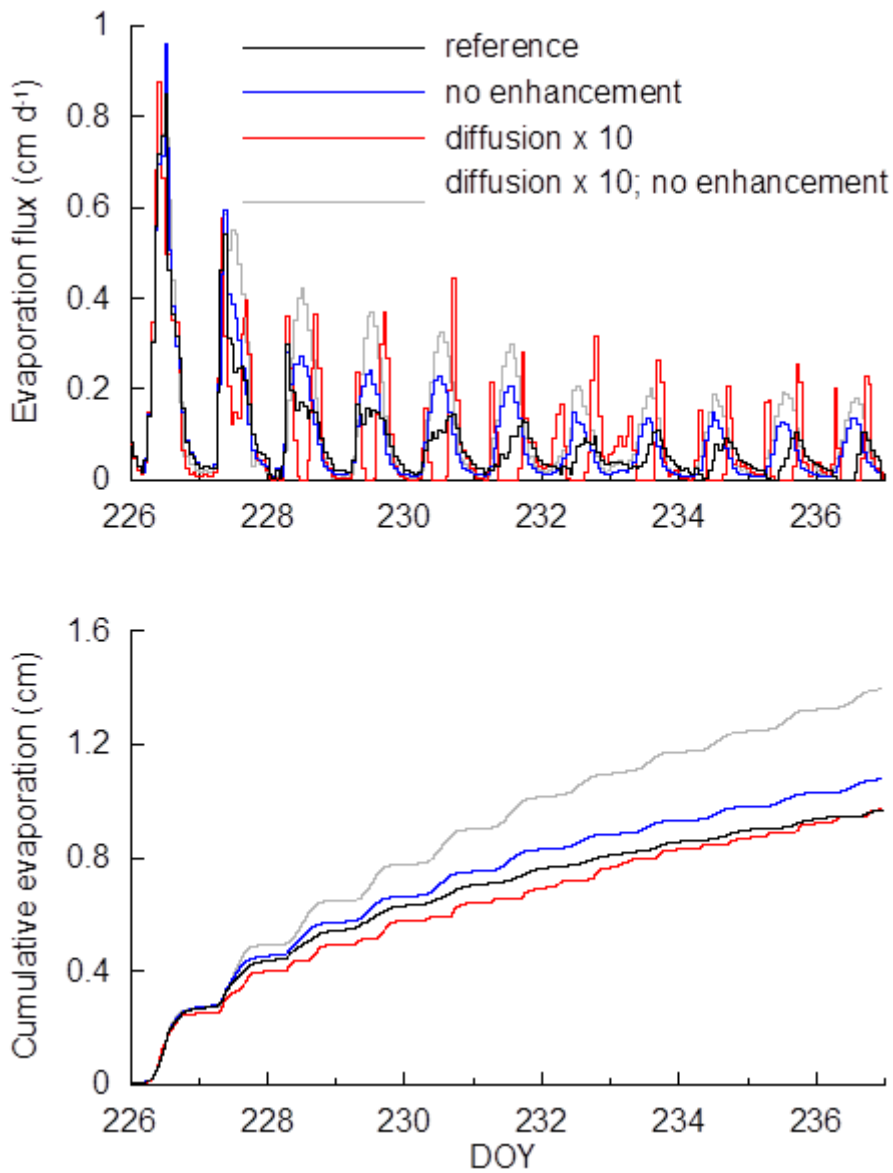
807

808 **Figure 18: Effect of surface roughness length, d , on simulated soil surface temperature of the silt soil. Top**

809 **panel shows surface temperatures over a 3-day period for $d = 2, 10$ and 100 mm. The bottom panel shows**

810 **the temperature difference between the surface with a 2 mm roughness and the other two surfaces.**

811



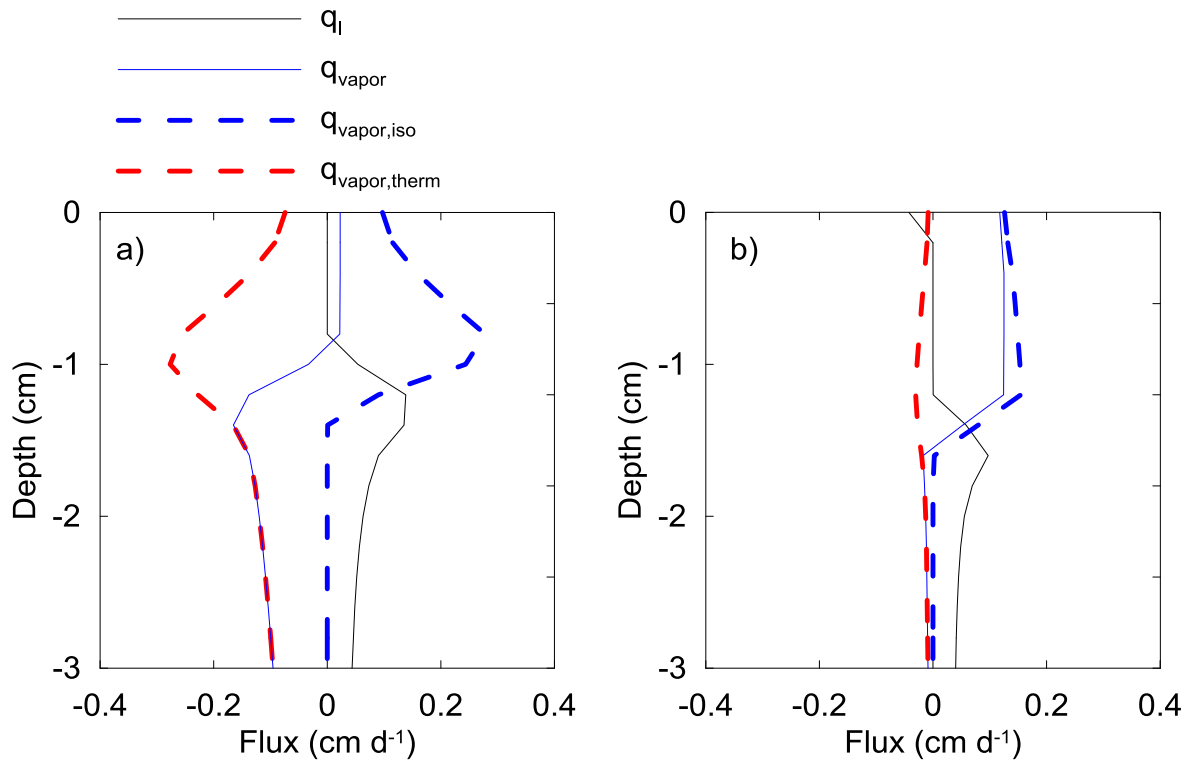
812

813 **Figure 19: Effect of enhancement factor and vapor diffusion on simulated evaporation (top panel) and**
814 **cumulative evaporation (bottom panel) from the sandy loam soil using the reference parameterization**
815 **(black line), an enhancement factor $\eta = 1$ for $K_{v,T}$, no-enhancement, blue line), a higher diffusion coefficient**
816 **for vapor transport in the air phase to account for turbulent pumping (diffusion x 10, red line), a higher**
817 **diffusion coefficient for vapor transport and an enhancement factor $\eta = 1$ (diffusion x 10, no enhancement,**
818 **grey line).**

819

820

821

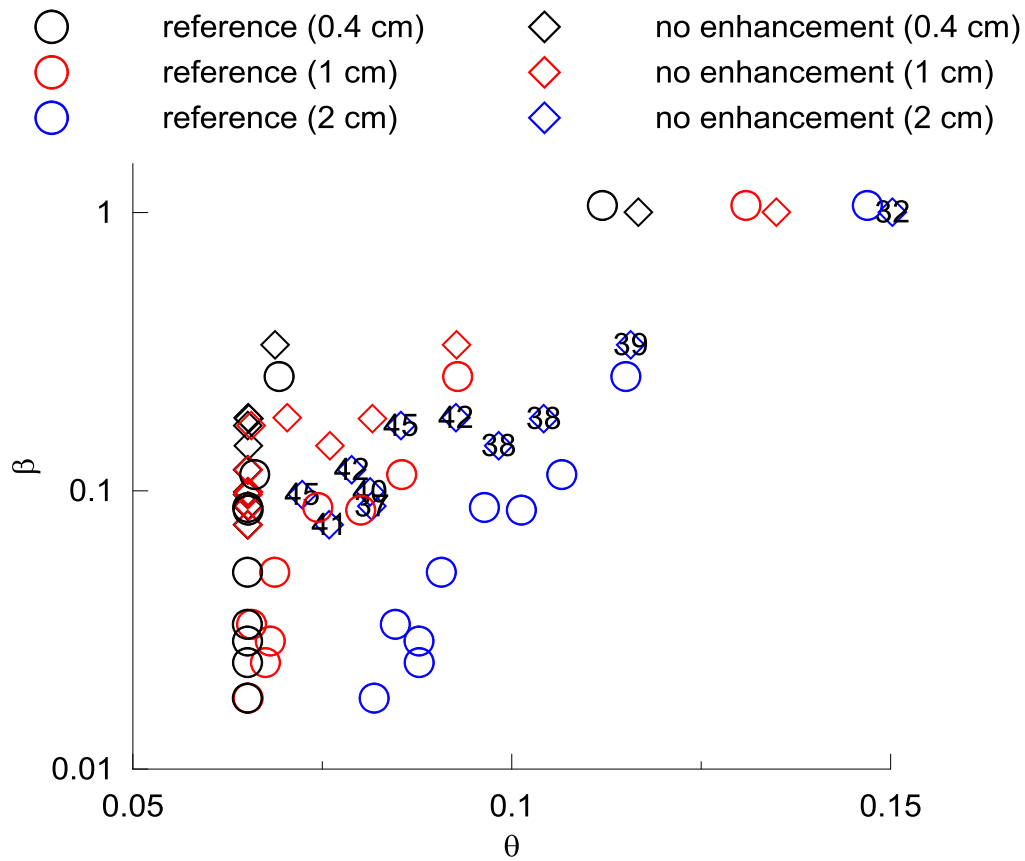


822

823 **Figure 20: Effect of enhancement factor and vapor diffusion on depth profiles of liquid water fluxes and**
 824 **isothermal and thermal vapor fluxes: a) reference case and b) no enhancement factor.**

825

826



827

828 **Figure 21: β factor that expresses the reduction of the soil evaporation as compared to the evaporation of a**
 829 **wet surface as a function of the water content of a top soil layer. Different colors refer to different thickness**
 830 **of the top soil layer and different symbols refer to simulations considering an enhancement of vapor fluxes**
 831 **due to a thermal gradient (circles) and simulations that do not consider this enhancement (diamonds).**
 832 **Labels in the blue diamond symbols refer to the average temperature in the surface layer.**

833

834 **References:**

835

836 Assouline, S., S. W. Tyler, J. S. Selker, I. Lunati, C. W. Higgins, and M. B. Parlange (2013),
837 Evaporation from a shallow water table: Diurnal dynamics of water and heat at the surface
838 of drying sand, *Water Resour. Res.*, 49(7), 4022-4034, doi: 10.1002/wrcr.20293.

839 Baber, K., K. Mosthaf, B. Flemisch, R. Helmig, S. Müthing, and B. Wohlmuth (2012),
840 Numerical scheme for coupling two-phase compositional porous-media flow and one-
841 phase compositional free flow, *IMA Journal of Applied Mathematics*, 77 (6), 887-909

842 Bastian, P., M. Blatt, A. Dedner, C. Engwer, R. Klöfkorn, M. Ohlberger, and O. Sander (2008a),
843 A generic grid interface for parallel and adaptive scientific computing. Part i: Abstract
844 framework, *Computing*, 82(2--3), 103-119.

845 Bastian, P., M. Blatt, A. Dedner, C. Engwer, R. Klöfkorn, R. Kornhuber, M. Ohlberger, and O.
846 Sander (2008b), A generic grid interface for parallel and adaptive scientific computing.
847 Part ii: Implementation and tests in dune, *Computing*, 82 (2--3), 121-138

848 Bechtold, M., J. Vanderborght, L. Weihermuller, M. Herbst, T. Gunther, O. Ippisch, R. Kasteel,
849 and H. Vereecken (2012), Upward transport in a three-dimensional heterogeneous
850 laboratory soil under evaporation conditions, *Vadose Zone J.*, 11(2), doi:
851 10.2136/vzj2011.0066.

852 Black, T. A., W. R. Gardner, and G. W. Thurtell (1969), Prediction of evaporation, drainage,
853 and soil water storage for a bare soil, *Soil Sci. Soc. Am. Proc.*, 33(5), 655-&.

854 Boesten, J. J. T. I., and L. Stroosnijder (1986), Simple-model for daily evaporation from fallow
855 tilled soil under spring conditions in a temperate climate, *Neth. J. Agric. Sci.*, 34(1), 75-
856 90.

857 Chanzy, A., L. Bruckler, and A. Perrier (1995), Soil evaporation monitoring - a possible
858 synergism of microwave and infrared remote-sensing, *J. Hydrol.*, 165(1-4), 235-259.

859 Dimitrov, M., J. Vanderborght, K. G. Kostov, B. Debecker, P. S. Lammers, L. Damerow, and
860 H. Vereecken (2015), Soil hydraulic parameters of bare soil plots with different soil
861 structure inversely derived from l-band brightness temperatures, *Vadose Zone J.*, 14(8),
862 doi: 10.2136/vzj2014.09.0133.

863 Flemisch, B., M. Darcis, K. Erbertseder, B. Faigle, A. Lauser, K. Mosthaf, S. Muthing, P.
864 Nuske, A. Tatomir, M. Wolff, and R. Helmig (2011), Dumux: Dune for multi-{phase,
865 component, scale, physics, ...} flow and transport in porous media, *Adv. Water Resour.*,
866 34(9), 1102-1112

867 Heitman, J. L., R. Horton, T. J. Sauer, and T. M. Desutter (2008a), Sensible heat observations
868 reveal soil-water evaporation dynamics, *J. Hydrometeorol.*, 9(1), 165-171, doi:
869 10.1175/2007jhm963.1.

870 Heitman, J. L., X. Xiao, R. Horton, and T. J. Sauer (2008b), Sensible heat measurements
871 indicating depth and magnitude of subsurface soil water evaporation, *Water Resour. Res.*,
872 44, doi: 10.1029/2008wr006961.

873 Helmig, R., and R. Huber (1998), Comparison of galerkin-type discretization techniques for
874 two-phase flow in heterogeneous porous media, *Adv. Water Resour.*, 21(8), 697-711, doi:
875 10.1016/s0309-1708(97)00023-7.

876 Lehmann, P., and D. Or (2009), Evaporation and capillary coupling across vertical textural
877 contrasts in porous media, *Phys. Rev. E*, 80(4), 046318, doi:
878 10.1103/PhysRevE.80.046318.

879 Li, N., L. Ren, and X. Yue (2015), Application and validation of an upscaling method for
880 unsaturated water flow processes in heterogeneous soils, *Vadose Zone J.*, 14(7), doi:
881 10.2136/vzj2014.12.0171.

882 Merz, S., A. Pohlmeier, J. Vanderborght, D. van Dusschoten, and H. Vereecken (2014),
883 Moisture profiles of the upper soil layer during evaporation monitored by nmr, *Water*
884 *Resour. Res.*, 50(6), 5184-5195, doi: 10.1002/2013wr014809.

885 Merz, S., A. Pohlmeier, J. Vanderborght, D. van Dusschoten, and H. Vereecken (2015),
886 Transition of stage i to stage ii evaporation regime in the topmost soil: High-resolution
887 nmr imaging, profiling and numerical simulation, *Microporous Mesoporous Mat.*, 205,
888 3-6, doi: 10.1016/j.micromeso.2014.10.035.

889 Millington, R., and J. P. Quirk (1961), Permeability of porous solids, *Transactions of the*
890 *Faraday Society*, 57(8), 1200-1207.

891 Milly, P. C. D. (1984), A simulation analysis of thermal effects on evaporation from soil, *Water*
892 *Resour. Res.*, 20(8), 1087-1098.

893 Moghadas, D., K. Z. Jadoon, J. Vanderborght, S. Lambot, and H. Vereecken (2013), Effects of
894 near surface soil moisture profiles during evaporation on far-field ground-penetrating
895 radar data: A numerical study, *Vadose Zone J.*, 12(2), -, doi: 10.2136/vzj2012.0138.

896 Novak, M. D. (2010), Dynamics of the near-surface evaporation zone and corresponding effects
897 on the surface energy balance of a drying bare soil, *Agric. For. Meteorol.*, 150(10), 1358-
898 1365, doi: 10.1016/j.agrformet.2010.06.005.

899 Parlange, J. Y., M. Vauclin, R. Haverkamp, and I. Lisle (1985), The relation between
900 desorptivity and soil-water diffusivity, *Soil Sci.*, 139(5), 458-461, doi:
901 10.1097/00010694-198505000-00012.

902 Ritchie, J. T. (1972), Model for predicting evaporation from a row crop with incomplete cover,
903 *Water Resour. Res.*, 8(5), 1204-&, doi: 10.1029/WR008i005p01204.

904 Saito, H., J. Simunek, and B. P. Mohanty (2006), Numerical analysis of coupled water, vapor,
905 and heat transport in the vadose zone, *Vadose Zone J.*, 5(2), 784-800, doi:
906 10.2136/vzj2006.0007.

907 Sakai, M., S. B. Jones, and M. Tuller (2011), Numerical evaluation of subsurface soil water
908 evaporation derived from sensible heat balance, *Water Resour. Res.*, 47, 17, doi: W02547
909 10.1029/2010wr009866.

910 Schlüter, S., H.-J. Vogel, O. Ippisch, P. Bastian, K. Roth, H. Schelle, W. Durner, R. Kasteel,
911 and J. Vanderborght (2012), Virtual soils: Assessment of the effects of soil structure on
912 the hydraulic behavior of cultivated soils, *Vadose Zone J.*, *11*(4), -, doi:
913 10.2136/vzj2011.0174.

914 Schwenck, N., M. Beck, B. Becker, H. Class, T. Fetzer, B. Flemisch, C. Grüniger, J. Hommel,
915 V. Jambhekar, A. Kissinger, T. Koch, M. Schneider, N. Schröder, G. Seitz, and K.
916 Weishaupt (2015), Dumux 2.8.0, doi: 10.5281/zenodo.31611.

917 Shahraeeni, E., and D. Or (2011), Thermo-evaporative fluxes from heterogeneous porous
918 surfaces resolved by infrared thermography, *Water Resour. Res.*, *46*, W09511, doi:
919 10.1029/2009wr008455.

920 Simunek, J., M. Sejna, H. Saito, M. Sakai, and M. T. van Genuchten (2008), The hydrus-1d
921 software package for simulating the movement of water, heat, and multiple solutes in
922 variably saturated media, version 4.08*Rep.*, 330 pp, Department of Environmental
923 Sciences, University of California Riverside, Riverside.

924 Šimůnek, J., M. T. van Genuchten, and M. Šejna (2016), Recent developments and applications
925 of the hydrus computer software packages, *Vadose Zone J.*, *15*(7), doi:
926 10.2136/vzj2016.04.0033.

927 Steenpass, C., J. Vanderborght, M. Herbst, J. Simunek, and H. Vereecken (2010), Estimating
928 soil hydraulic properties from infrared measurements of soil surface temperatures and tdr
929 data, *Vadose Zone J.*, *9*(4), 910-924, doi: 10.2136/vzj2009.0176.

930 Tolk, J. A., S. R. Evett, and R. C. Schwartz (2015), Field-measured, hourly soil water
931 evaporation stages in relation to reference evapotranspiration rate and soil to air
932 temperature ratio, *Vadose Zone J.*, *14*(7), doi: 10.2136/vzj2014.07.0079.

933 Van Bavel, C. H. M., and R. J. Reginato (1965), *Precision lysimetry for direct measurement of*
934 *evaporative flux*, 129-135 pp., United Nations Educational, Scientific, and Cultural
935 Organization, Paris.

936 van Genuchten, M. T. (1980), A closed-form equation for predicting the hydraulic conductivity
937 of unsaturated soils, *Soil Sci. Soc. Am. J.*, 44(5), 892-898.

938 van Keulen, H., and D. Hillel (1974), Simulation study of drying-front phenomenon, *Soil Sci.*,
939 118(4), 270-273.

940 Yang, G. J., R. L. Pu, C. J. Zhao, and X. Z. Xue (2014), Estimating high spatiotemporal
941 resolution evapotranspiration over a winter wheat field using an ikonos image based
942 complementary relationship and lysimeter observations, *Agric. Water Manage.*, 133, 34-
943 43, doi: 10.1016/j.agwat.2013.10.018.

944

945